UNIVERSITY OF BIRMINGHAM

School Of Chemistry

Degree: MRES in materials chemistry, nanochemistry

Investigating the controlled oxidation of manganese oxides with the Brownmillerite structure

Nilupa Hassan

[redacted]

July 2009

Supervisor: Dr A J Wright

ABSTRACT

Brownmillerite structures have received much attention due to their defect perovskite structure and potential for interesting magnetic behaviour and ionic conductivity. This thesis describes an initial investigation into the potential of manganese containing Brownmillerite phases, with the stoichiometry $(Sr_{2-x}Ca_x)MnGaO_{5+\delta}$, to display significant mixed conductivity and interesting magnetic properties by forming mixed manganese valence. Significant mixed valency in manganese has not previously been reported in Sr_2MnGaO_5, Ca_2MnGaO_5 or $SrCaMnGaO_5$. Oxidation of Sr_2MnGaO_5, nominally Mn^{3+} to $Sr_2MnGaO_{5.5}$, nominally Mn^{4+}, occurs rapidly without intermediates, whereas both Ca_2MnGaO_5 and $SrCaMnGaO_5$ show no significant oxidation at atmospheric pressure. This work centres on the solid solution between these extremes to analyse structural changes and the potential for partial oxidation of manganese. Neutron diffraction has been carried out on these samples to investigate the structures and oxygen uptake.

KEYWORDS

Brownmillerite

Perovskite

Magnetoresistance

(Anti)Ferromagnetic

Neutron Diffraction

$Sr_{2-x}Ca_xMnGaO_5$

ACRONYMS

X-ray diffraction (XRD)

Magnetoresistance (MR)

Neutron powder diffraction (NPD)

Contents

1 Introduction

This study involves research into a family of Perovskite related phases with the Brownmillerite structure, which show interesting magnetic properties. These materials appear to display variations in their oxidative behaviour with changes in stoichiometry. This work seeks to investigate these materials to optimise magnetic properties and potential oxide ion conductivity. These materials could have potential for magnetoresistive materials or as mixed conductors in solid oxide fuel cells.[1]

The physical properties of the doped perovskite involve a complex interplay between the spins of the electrons, charge, orbital and lattice degrees of freedom. These strongly depend on the occupancy of d orbital. The basic building block of manganites is the MnO_6 octahedra.[2]

1.1 Magnetoresistance and Magnetism

Magnetoresistance (MR) is the change in the electrical resistivity of a material on the application of an external magnetic field. The equation is shown below.

Eq.1 [2]

$$MR\% = \frac{\Delta\rho}{\rho_O} x100 = \left[\frac{\rho_O - \rho_H}{\rho_O}\right] x100$$

ρ_H and ρ_0 are the Resistivities in applied and zero magnetic fields. MR can be positive or negative depending on the increase or decrease of resistivity. Most metals show MR ranging from a 0.05 % to 260%, depending on the strength and orientation of the applied magnetic field. Iron and cobalt usually exhibit high MR and is 15% higher than silver.[2] Bismuth is a semimetal and exhibits 18% MR in a transverse field of 0.6 Tesla which rises to a 40% change at 24 Tesla. MR originates from the impact of the Lorentz force on the moving charge carriers which is similar to the Hall Effect. These materials are useful for their use as magnetic media disks, data storage,

magnetic field sensors and read heads. The most ambitious goal for scientists is to achieve higher aerial density which is the number of bytes per unit area on a disk surface. This requires development in materials performance and miniaturisation of the components.

Giant MR was initially discovered in a molecular beam epitaxial film where chromium was sandwiched between iron layers to form a layered structure. It was then found that polycrystalline iron/chromium multilayers showed a higher effect, while cobalt and copper showed an even higher MR effect at room temperature. When the relative orientations of grains are anti-parallel it does not result in conductance. However when the grains are forced parallel in application of magnetic field, conductivity increases.

Colossal magnetoresistance (CMR) is a type of MR developed in the last decade, principally from manganese perovskites. The term colossal was named by Jin et al[3], as it was very different to the GMR. It was discovered by Jonker and Santen[4] who observed CMR in $La_{0.8}Sr_{0.2}MnO_3$. Neutron diffraction was carried out by Woolan and Koehler[5] to characterise the magnetic ordering. CMR emerged from the perovskites that were mentioned above and it is this phenomenon that is of much interest to scientists. CMR materials could be used as conductors as well as magnetic recording materials.

Magnetism occurs from the spin of an electron. Most materials have electrons which are randomly orientated spins which leaves no magnetic effect overall. When the electron spins are aligned in the same direction they interact cooperatively and create a net magnetic field. A current of electrons travelling through a wire creates a magnetic field. There are several forms of magnetic behaviour. A ferromagnetic component is one which has all the electron spins aligned in the same direction. They can exhibit a net magnetic moment in the absence of an external magnetic field. A ferromagnetic component would create a magnetic field in the opposition of an externally applied magnetic field, which results in a repulsive effect.

Paramagnetism occurs only in the presence of an externally applied magnetic field and involves unpaired electrons. The Electrons do not retain any magnetism in the absence of an externally applied field. Electrons have a magnetic moment μ. One component of the moment is associated with the spin angular momentum of the electron S, $S = \sqrt{s(s+1)}$, the other component is with the orbital angular momentum, l, $l = \sqrt{l(l+1)}$. Here the spin only equation is used, as in most cases the orbital angular momentum is quenched. μ can be determined by the number of unpaired electrons n, $\mu = \sqrt{n(n+2)}$. The effective magnetic moment can be obtained from the measured molar magnetic susceptibility.

Antiferromagnetic superexchange is the process where magnetic ions are coupled in an antiparallel arrangement often via oxygen 2p orbitals. This occurs at low temperatures and discontinuing at a certain temperature known as the Neel temperature. Above this temperature the material is usually paramagnetic.

Jonker and Santen[4] discovered the strong correlation between ferromagnetism and metallic conductivity in doped manganites now known as double exchange. Zener carried out qualitative research and interpreted ferromagnetism as arising from an indirect coupling between incomplete d shells on Mn^{3+} and Mn^{4+} via conducting electrons of oxygen's. The initial state of Mn^{3+}-O-Mn^{4+} and the final state Mn^{4+}-O-Mn^{3+} are degenerate leading to a delocalisation of the hole on the Mn^{4+} site or electron on the Mn^{3+} site. The transfer of electrons occurs simultaneously from Mn^{3+} to O^{2-} and from O^{2-} to Mn^{4+}. This process is a real charge transfer process and is accounted for by the overlap integral between manganese 3d and oxygen 2p orbitals. Due to the strong coupling of Hund's rule, orbitals need to be occupied with parallel spins before they can be paired up. If the core spins are ferromagnetically aligned they will lead the system into simultaneous occurrence of metallicity and ferromagnetism. [2]

1.2 Jahn Teller Effect

In the cubic environment of MnO_6 octahedron the hybridisation and electrostatic interaction with oxygen 2p electrons will create a crystal field for the outer 3d electrons in Mn^{3+}. The d orbital has 5 degenerate states, the crystal field lifts the fivefold degeneracy of d electrons present in free Mn^{3+} ions by splitting the energy levels into lower lying triply degenerate t_{2g} state and higher doublet e_g state. This is shown in **figure 1**.

The low lying t_{2g} state consists of the dxy, dyz and dxz orbitals. The orbitals have lobes oriented between the O^{2-} ions. The e_g orbitals consist of dx^2-y^2 and dz^2 which have lobes pointing in the direction of the O^{2-} ions. This raises the energy due to the stronger columbic repulsions between the oxygens and the manganese of the MnO_6 octahedra which are present in perovskites.

For example in $LaMnO_3$ the energy difference due to crystal field splitting is 1.5 eV. This is due to the strong intra atomic Hund's coupling. All electrons of Mn^{3+} and Mn^{4+} are aligned parallel in the ground state. This gives a total spin of S=2 and S=3/2. Three outer electrons of Mn^{4+} occupy t_{2g} sites whereas the extra electron occupies the e_g site. The t_{2g} orbital overlaps little with the p orbitals of nearby oxygen atoms. The t_{2g} electron forms a localised core spin S=3/2. The e_g orbitals overlap with the p orbital of neighbouring oxygen orbital atoms. The e_g electron is more mobile and can hop between different manganese ions, therefore the partial degeneracy of the 3d orbitals are removed by crystal field splitting. The remaining degeneracy is usually broken down by lattice motion. The oxygen ions surrounding the Mn^{3+} ion can readjust slightly from their locations which creates an asymmetry between the different directions which will effectively remove the degeneracy. This orbital lattice interaction creates a lift in degeneracy and is known as the Jahn Teller effect. This occurs spontaneously for the reason that it is energetically favourable. Manganites have 21 modes of vibration for the movement of oxygen and manganese ions, However only two types of distortions occur. Q3 is a tetragonal distortion and results

in elongation or contraction of the MnO_6 octahedra. Lattice distortion of octahedra can be static or dynamic. The distribution of Mn^{3+} and Mn^{4+} ions are random and changes with time.[2] The presence of Jahn-Teller active Mn^{3+} in many CMR materials adds an extra complexity to the simple 'double exchange' description of CMR. [6]

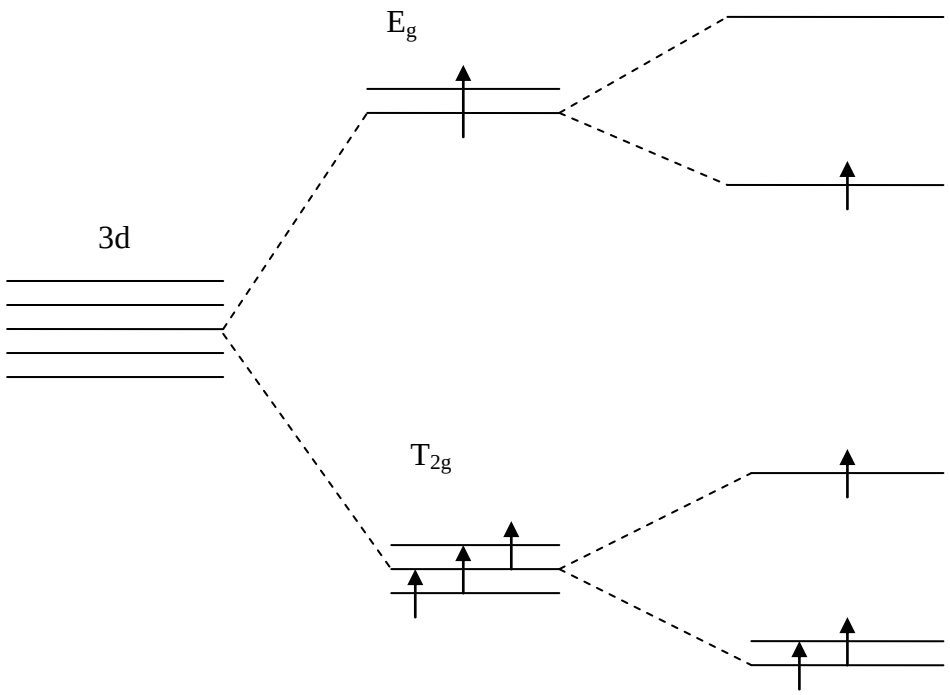

Figure 1
The splitting of the T_{2g} and the E_g level is due to the Jahn-Teller distortions

1.3 The Perovskite Structure, ABO_3

The perovskite structure is one of the most important structure types in solid state chemistry. It is able to display many technologically important properties, such as superconductivity, oxide ion conductivity, thermoelectricity, and colossal magnetoresistance, (CMR).

The perovskite structure has a composition of ABX_3. The A cation is usually a lanthanide or an alkaline metal, whereas the B cation is often a transition metal and the X is oxygen. The basic structure is a primitive lattice, with corner sharing BO_6 octahedra, and the A cation situated in the centre of the cell. The unit cell can be seen in **figure 2**.

Perovskite phases containing manganese have been shown to exhibit magnetoresistive properties, particularly colossal magnetoresistance. These phases are related to $LaMnO_3$ which is an antiferromagnetic insulator, however it was found that when the A^{3+} cation was doped with 2+ cation, for example in $La_{0.7}Ca_{0.3}MnO_3$, the material demonstrated ferromagnetism and high conductivity in a magnetic field. These materials display physical properties which involve complex interplay between the spins, charge, orbital and occupancy of their d-orbitals. [7, 4]

Perovskites such as $La_{0.7}Ca_{0.3}MnO_3$ show CMR in high magnetic fields, however this is not useful as such high fields are impractical and difficult to achieve in applications. For this reason these perovskites are limited in their use and applications at present.

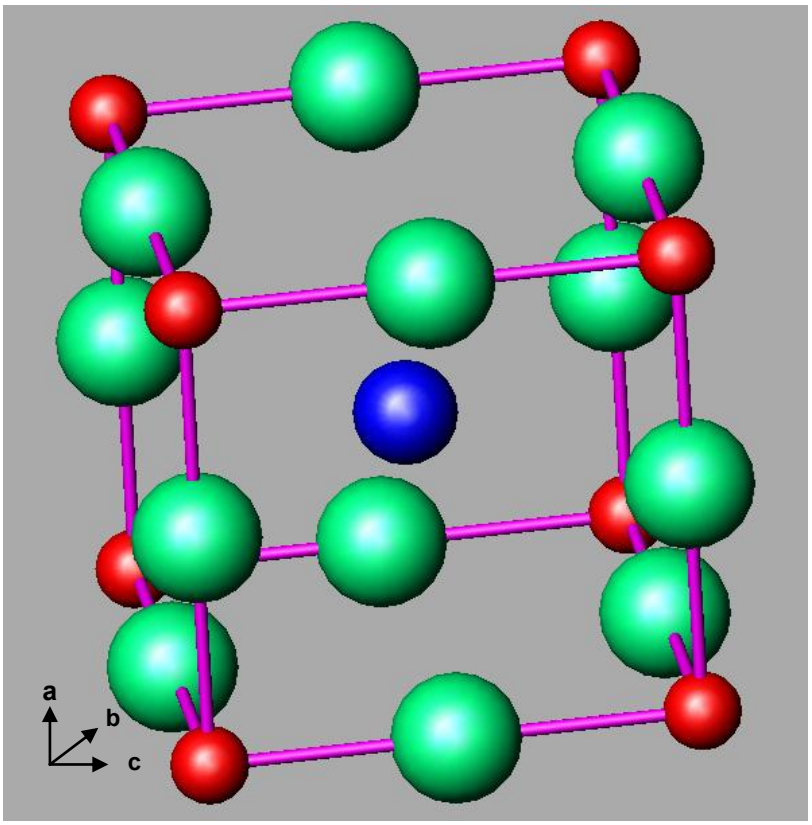

Figure 2
Perovskite crystal lattice ABO_3
A= blue, B= red, oxygen, O= green

The CMR behaviour of doped perovskites can, to a first approximation, be described by the double exchange mechanism. The interaction which occurs is namely the Zener double exchange mechanism between the Mn^{3+} and Mn^{4+} ions via the oxygen 2p orbitals. This is shown in **figure 3**.

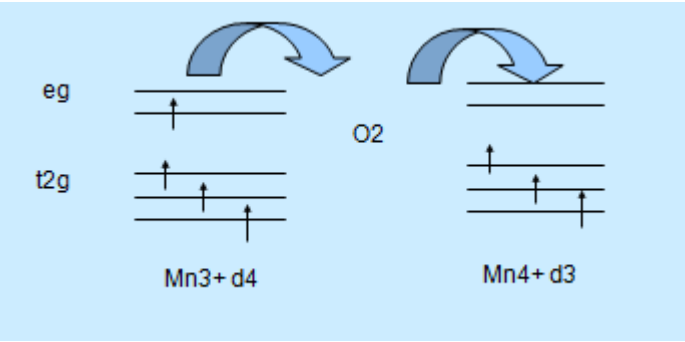

Figure 3
Double exchange mechanism

$LaMnO_3$ is an insulator as the manganese charge is Mn^{3+}. Electrons hopping from Mn^{3+} to Mn^{3+} is a high energy process and does not occur spontaneously. In $CaMnO_3$ the charge of manganese is Mn^{4+} which leaves both end members to be insulators. However, in the solid solution with stoichiometry $La_{0.7}Ca_{0.3}MnO_3$, the manganese charge has a mixed valence of $Mn^{3.3+}$, making such compositions excellent conductors and able to exhibit magnetoresistance in a magnetic field. Calcium has also been used to replace lanthanum and provide very high tunnelling MR in $La_{0.66}Ca_{0.33}MnO_3$. [8, 9]

The trivalent lanthanide (cation A) has also been replaced by two alkaline earth metals, barium and strontium. The structure of $La_{0.67}(Sr_{1-x}Ba_x)_{0.33}MnO_3$ is rhombohedral at x=0, this however changes to orthorhombic at x=1. Low field and high field effects were observed for all samples. From x=0.75 and x=0.1, low field MR vanishes at 300K. The highest CMR effect is observed at x=0.25 at 100K. [4]

$Nd_{1-x}Sr_xMnO_3$ has been studied and showed a very large CMR behaviour. Interestingly, in the region x=0.5 orbital order occurs with the formation of equal amounts of $Mn^{3+/4+}$. At x=0.52-0.63 antiferromagnetic ordering occurs whereas MR occurs at the phase boundary of x=0.625. [10]

The properties of such perovskites can be accounted for by the correlation between the structures electronic and magnetic properties and these are strongly related to the ratio of the Mn^{3+} and Mn^{4+} ions. the presence of the Mn3+ ions are an essential feature of double exchange. The cubic or pseudo-cubic materials presented so far require high magnetic fields to induce significant changes in electrical resistivity. The study of perovskites that can exhibit low field MR is a target of solid state chemists. It has been found that some layered structures with the Ruddlesden Popper structure are able to display low field CMR. This has led to much interest into the development of layered structures which contain magnetic ions.

Ruddlesden Popper phases, which have the formula $A_{(n-1)}B_nO_{3(n+1)}$, are related to the perovskite structure and show an extensive range of structural, electrical and magnetic properties and more interestingly low field CMR. The observation of CMR in these phases encouraged research into the synthesis of other manganese containing oxides which possess layered crystal structure. Another interesting series of layered manganites possesses the Brownmillerite structure. [2]

1.4 Brownmillerite

Previous research into CMR materials showed that layered structures may be able to enhance low field CMR. Brownmillerites are similar to Ruddlesden Popper structures in that they are layered structures related to the perovskite structure, but instead of the presence of a rock-salt structured layer between the perovskite regions, Brownmillerites possess an ordered oxygen deficient region. This leads to a structure consisting of $A_2B_2O_{5+S}$ with alternating layers of BO_6 octahedra and BO_4 tetrahedra. This contrasts with the ideal perovskite structure ABO_3 which possesses only BO_6 octahedra. [11]

Many types of Brownmillerites have been discovered, e.g. Ca_2FeAlO_5[7], Ca_2GaFeO_5,[12] $Sr_2Fe_2O_5$ [13], $La_2Co_2O_5$[14], and $Sr_2Co_2O_5$ [15] and $Ba_2In_2O_5$.[16] Much interest has been centred on the oxide ion conduction of $Ba_2In_2O_5$ via the oxygen deficient layers[12]. Brownmillerites of manganese are of particular interest due to their potential in forming mixed manganese valence Mn^{3+}/Mn^{4+} phases, which could have useful magnetic properties and potential as mixed conductors for use as electrodes in fuel cells. The orthorhombic unit cell of the Brownmillerite structure is shown in **figure 4**.

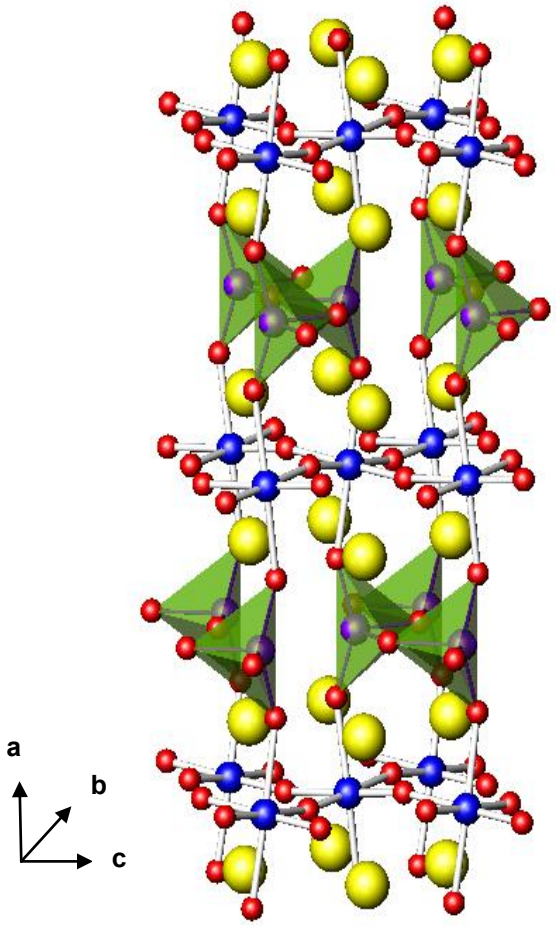

Figure 4

Structure of Brownmillerite showing MnO_6 octahedra and BO_4 tetrahedra (green pyramid) and A cation (yellow sphere)[17]

1.4.1 Distortion of the Brownmillerite

This study will focus on the Brownmillerites phases Sr_2MnGaO_5 and Ca_2MnGaO_5 which consist of alternating layers of MnO_6 octahedra and GaO_4 tetrahedra with two different B cations.

Oxygen vacancies which occur are ordered in the GaO layer so alternating diagonals of oxygens are not present. This causes a distortion of the perovskite structure and the formation of GaO_4 tetrahedral chains, as the Ga moves to the centre of a tetrahedron, the two oxygens are displaced in the opposite direction. These distortions result in two possible chain orientations for a given GaO_4 tetrahedral chain. The distortion also causes the MnO_6 octahedron to angle slightly from it's original position, leading to the distorted Brownmillerite structure.[18, 19]

The distortions of tetrahedra can occur in two different directions, clockwise or anticlockwise. Tetrahedra in a layer of chains which are adjacent to one another will encounter the opposite direction of rotation alternately. This forms two different orientations and are indicated by direction left and right. Different orientations of these give rise to the three space groups observed for the Brownmillerite structure. (**Figure 5)**

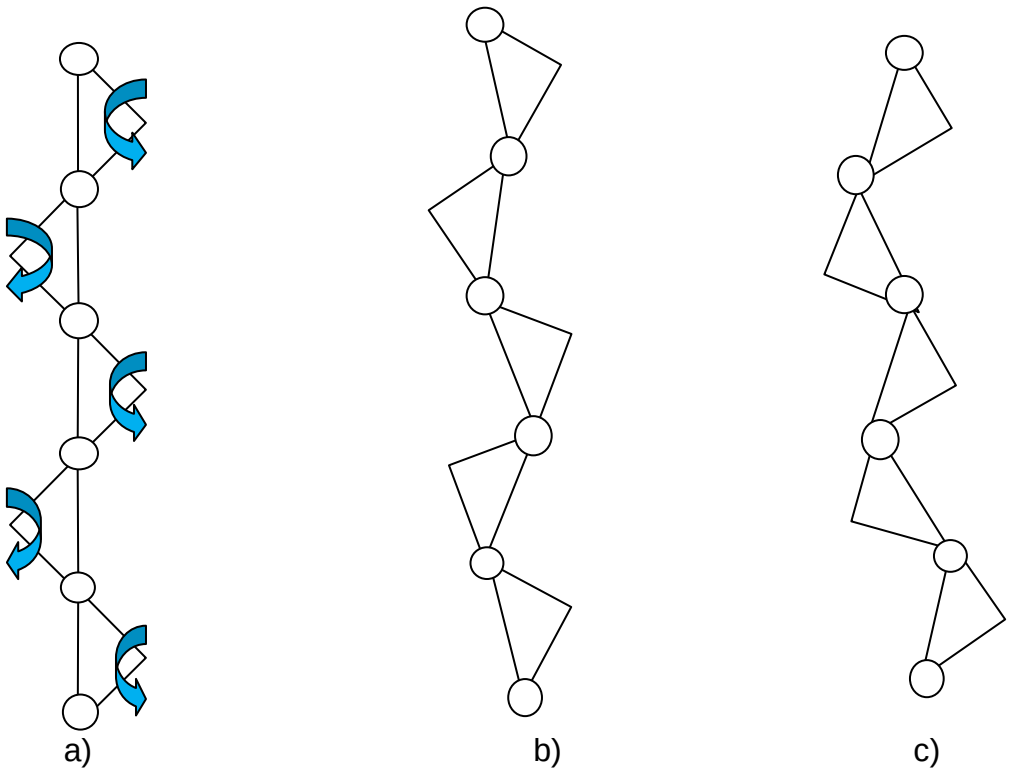

Figure 5

Representation of distortions of the tetrahedral chains in the brownmillerite structure (a) Undistorted chains of GaO_4, (b) left chain distortion, (c) right chain distortion

Abakumov et al [20] have discussed the possible reasons behind the formation of these different orientated chains, considering the dipole interaction between atoms along the chain. The energy of the dipoles of the left chain with the anti-parallel dipole of the right chain depends on the degree of chain distortion and the distance between the tetrahedral layers. Both of these parameters are influenced by the size of cation B. Cation B plays an important role in the crystal chemistry and structural behaviour of the Brownmillerite phase. Left orientated chains are shown in **figure 6**. Also, different sized atoms in either A site or B site can lead to varied bond lengths and angles and differences in the arrangement and ordering of the tetrahedral chains. These differences give rise to a range of possible space groups for the Brownmillerite structure.

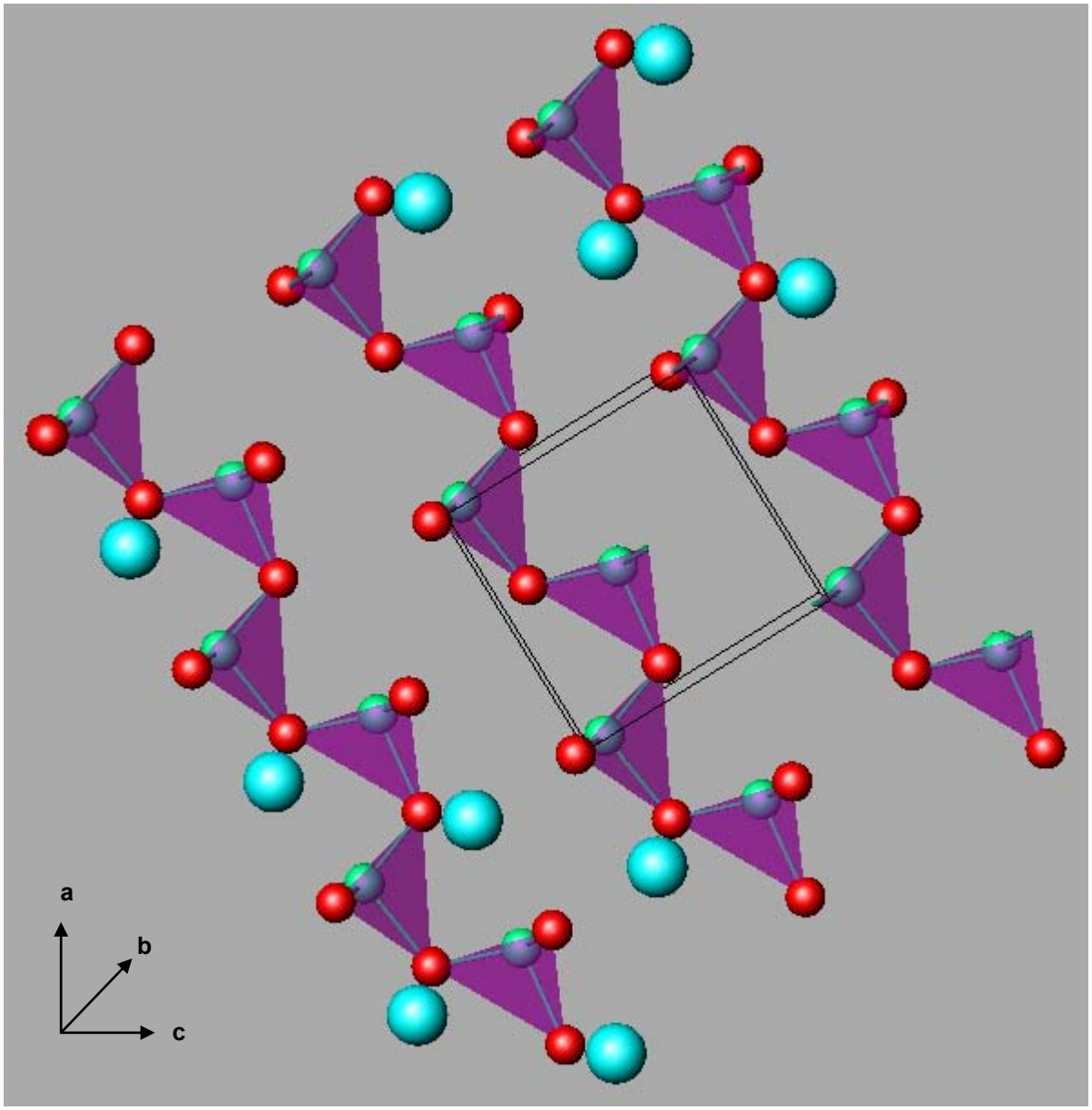

Figure 6
Left orientated tetrahedral chains
in Brownmillerite structure

1.4.2 Brownmillerite space groups

Space groups are the collective symmetry of a crystal structure. Three space groups are possible in the Brownmillerite series and these depend on the relative arrangement of the tetrahedral chains. The Sr_2MnGaO_5 phase has been shown to adopt the *Icmm* space group, which shows a random arrangement of the tetrahedral chains[20]. *Ibm2* space group adopts more ordered arrangement than the *Icmm* space group, this is more often observed for the mixed phases of strontium and calcium[19]. The final space group occurring in this series is the *Pcmn* primitive space group, adopted by the Ca_2MnGaO_5 phase, which possesses another ordered arrangement of the GaO_4 chains. [21, 22, 23, 24]

Therefore, two different space groups are observed for the two phases, Sr_2MnGaO_5 and Ca_2MnGaO_5. Although it is fairly easy to distinguish these two extremes, mixtures of the type $(Sr,Ca)_2MnGaO_5$ are not well understood as there is some difficulty in assigning the space groups. It is not obvious at which stoichiometries the intermediate space group *Ibm2* exists.

The space group *Icmm* does not have any consecutive ordering of the tetrahedral layers. In a layer of tetrahedral chains, if one layer is the left analogue, than the layer above and below can be either left or right. The intermediate ratios adopt the *Ibm2* space group where all layers are one type, either left or right. Neutron powder diffraction (NPD) has shown that the *Ibm2* space group is present in the one to one ratio of $SrCaMnGaO_5$. Powder XRD data can be used to suggest space groups for these intermediate regions but cannot be absolutely certain as much relies on the accurate determination of the oxygen positions, which is better achieved using NPD.

The Ca_2MnGaO_5 structure adopts the same chain order as the *Ibm2* however the layers of the chain define a primitive cell, leading to the *Pcmn* space group.

In $Ca_2Mn_2O_5$, Replacing one of the manganese B cations for aluminium shows structural differences. Ca_2AlMnO_5 shows a decrease in tetrahedral chain distortion, and has a space group of *Ibm2*. The b lattice parameter increases going from Sr_2MnGaO_5 to Sr_2AlMnO_5. The Mn-O2-Ga/Al bond angle is larger for Sr_2MnGaO_5 than the calcium version. This accounts for the different space groups observed for the varied B cations.

1.4.3 Sr_2MnGaO_5

Sr_2MnGaO_5 has been studied and has been found to consist of alternating MnO_6 octahedra and GaO_4 tetrahedra with the strontium in the A-cation positions. The oxygen vacancies have been shown to occur in the GaO layers according to neutron diffraction data,[19] this is due to the smaller size of gallium stabilizing the tetrahedral coordination, while the slightly larger Mn^{3+} prefers the octahedral coordination. The manganese charge in this composition is calculated to be Mn^{3+}; which is unlikely to support electronic conductivity by a hopping mechanism because of the resulting formation of Mn^{2+} and Mn^{4+} which is likely to be a high energy process. The material is found to possess antiferromagnetic ordering at low temperature due to superexchange interaction within the MnO_2 layers.[19, 20 ,24]

The anion vacancies form chains along the *110* direction of the primitive cubic perovskite cell which results in the orthorhombic structure with one long parameter and two shorter parameters. The anion vacancies are ordered to create a tetrahedral co-ordination of the B cations, which is gallium. This is a smaller cation than manganese and prefers a tetrahedral environment. The slightly larger manganese forms octahedral co-ordination. The combination of these sites allow for interesting physical properties of the octahedra to be accompanied by Jahn Teller distortions. The BO_4 tetrahedra share common corners and form chains along *110*.[25, 26, 27]

NPD has revealed the space group which best describes the structure of Sr_2MnGaO_5 to be of the space group *Icmm* with lattice parameters of: *a*=5.4888(2)Å,

b=16.2256(6)Å and *c*=5.35450(2)Å at 2K, and the compound has a Neel temperature of 183K [19]. The oxygen vacancies in the tetrahedral layers order such that the tetrahedra form corner linked chains running along the *001* direction. The neutron powder diffraction analysis revealed a small degree of Mn-Ga mixing of 5%. The description of Sr_2MnGaO_5 based on the *Icmm* space group disagrees with the XRD powder diffraction study reported by Abakumov et al,[25] where it is claimed that the structure is best represented by the *Ibm2* space group so therefore having complete 3 dimensional order in the arrangement of GaO_4 chains. This does however seem to be inconsistent with the High Resolution Electron Microscopy (HREM) study in the same report where layers containing local areas of alternating GaO_4 chain orientations were suggested. The space group assignment was a difficult task when based on XRD data alone. So the data based on NPD can be a more reliable study which is in agreement with the HREM data, and implies bulk disorder in chain orientation.

In the centrosymmetric *Icmm* space group there is an alternation of the left and right chains with equal probability giving a disorder in the GaO positions in the gallium layer. This has then been reported in agreement by Abakumov et al [25] where the thermal parameters and data do seem a better fit with the *Icmm* space group. The compound is shown to order antiferromagnetically between the planes and in the oxidised form the magnetic moments order ferromagnetically. In the reduced form (110/011) and (031/130) magnetic Bragg peaks are observed which are expected for antiferromagnetic type structures with the absence of (100/001) and (120/021) which would relate to a ferromagnetic type structure. For the oxidised version there are only ferromagnetic type peaks visible. The superexchange paths occur via the dz^2 orbital on the Mn^{3+} and the 2p orbital on the oxygen ions, these orbitals overlap with sigma bonding.

1.4.4 Ca_2MnGaO_5

Ca_2MnGaO_5 exhibits the space group *Pcmn*. It possesses antiferromagnetic interactions and consists of solely Mn^{3+} ions. This phase has been shown to have a significantly smaller unit cell than Sr_2MnGaO_5. It is also interesting to note that these two different parent phases behave in different ways with respect to oxygen uptake. The strontium phase readily takes up oxygen at ~400°C to apparently oxidise all the Mn^{3+} to Mn^{4+} and give stoichiometry of $Sr_2MnGaO_{5.5}$, whereas the calcium phase does not take up any oxygen in these conditions. By mixing the two alkaline earth metals together some interesting properties are expected to be seen. [4, 12, 28, 29,]

1.4.5 $SrCaMnGaO_5$

The room temperature crystal structure of $SrCaMnGaO_5$ has also been refined from NPD and belongs to space group *I2bm* with parameters of: *a*=15.7817(6) Å, *b*=5.4925(2) Å, and *c*=5.3196(2) Å [24] (**figure 7**). The manganese and gallium occupancy is 99.02% of the relevant sites. NPD and magnetometry has shown the compound orders magnetically at 180K. The low temperature phase has an antiferromagnetic structure with an ordered magnetic moment of 3.302μ_B per manganese at 2K. A displaced hysteresis loop provides evidence that the atomic moment has a supplementary glassy component. The compound is an insulator however at 159 K shows a large MR of 95% in a field of 6 Tesla.

The NPD of $SrCaMnGaO_5$ suggests the tetrahedra adopt an ordered arrangement with the same orientation in every layer and the structure is best described by the *I2bm* space group. There is evidence of a magnetic phase transition with discrepancy between the field coolled and zero field coolled data suggesting that the magnetic phase is a weak ferromagnet.

Sr_2MnGaO_5 possesses less ordered tetrahedral chains and adopts the space group *Icmm*, however there is not much differentiation for the aluminium analogue which

adopts the same disordered space group. The distances between the tetrahedral layers increase progressing from the strontium phase to the calcium phase, with either gallium or aluminium tetrahedra. There is more three dimensional order in Ca_2MnAlO_5 due to the small separation between the aluminium layers. Whereas in Sr_2MnGaO_5 there is a larger gap and there are small amounts of manganese found on gallium sites which have effects disrupting the chain ordering.

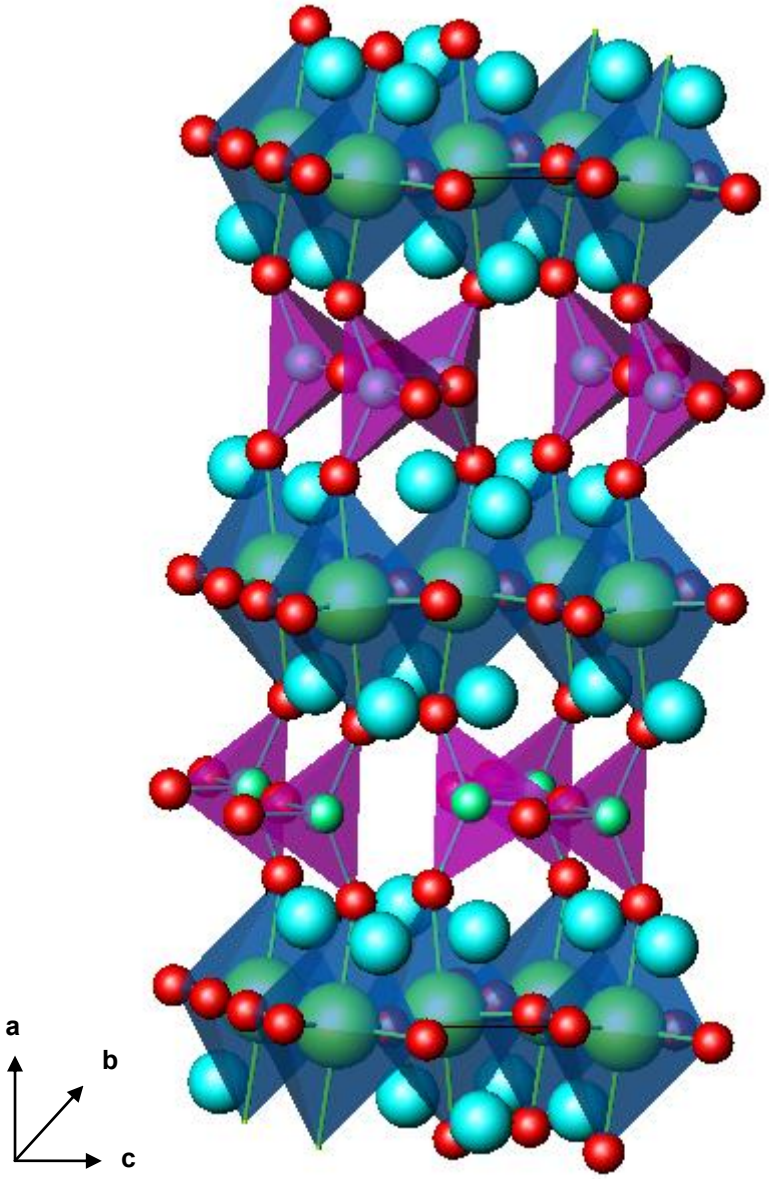

Figure 7

Structure of the *Pcmn* space group, showing the octahedral (dark blue) layers and the tetrahedral layers (purple)

1.5 Oxygen uptake

Sr_2MnGaO_5 and Ca_2MnGaO_5 have been studied for their oxidation behaviour. The strontium phase, when heated in air at 600° C for 30 minutes uptakes oxygen to form $Sr_2MnGaO_{5.5}$ where the Mn^{3+} converts to purely Mn^{4+}. Interestingly the same treatment of Ca_2MnGaO_5 shows no evidence of oxygen uptake. As these two compositions have been studied and show differences in oxygen uptake, it is feasible that in the solid solution between these extremes, there will be a region where oxygen uptake will occur at an intermediate level, (i.e. between 5 and 5.5). If a mixed $Mn^{3+/4+}$ state can be formed in the $Sr_{2-x}Ca_xMnGaO_{5+d}$ system, it could exhibit ferromagnetic properties, leading to uses as magnetoresistors. Also it could be used in solid oxide fuel cells (SOFC) as electrode materials which require mixed conductivity. Mixed valent brownmillerites should have the ability to allow oxygen ions to travel through the structure via the significant oxygen vacancies in the tetrahedral layers. They should also possess the movement and conduction of electrons between Mn^{3+} and Mn^{4+}. Materials which show both of these properties simultaneously are known as mixed conductors. [5, 6, 30, 31]

1.5.1 Fuel Cells

With the global climate change and limited renewable resources there is extensive demand to produce clean, efficient and environmentally friendly energy sources. In 1962 Siemens Westinghouse demonstrated the ability to extract electricity from the SOFC. Since then there has been extensive research and development to invent the alternative energy technology known as the fuel cell. This system uses hydrogen, methane or butane and converts it to electrical energy and having water as the waste product as well as CO_2 is the fuel is a hydrocarbon.[32] SOFC's are able to convert a wide variety of fuels into energy at a high efficiency of 40-60% unassisted with any pressure and 70% in pressurized hybrid system. [33, 34]

Fuel cells carry out electrochemical reactions to convert chemical energy into electrical energy. They consist of a catalyst, electrolyte and electric circuit, (**Figure 8**). Oxygen gas is put into the system through the cathode electrode which requires four electrons to split it into oxygen ions. The oxygen ions diffuse into the electrolyte material and migrate to the other side of the cell to the anode. At the anode the oxygen ions and hydrogen atoms electrochemically combine and produce water as the output product. The flow of electrons creates the electrical energy and flows through to the cathode catalyst. The Brownmillerite oxides which will be studied in this report could potentially act as a solid oxide electrode which can conduct electrons and ions. [33]

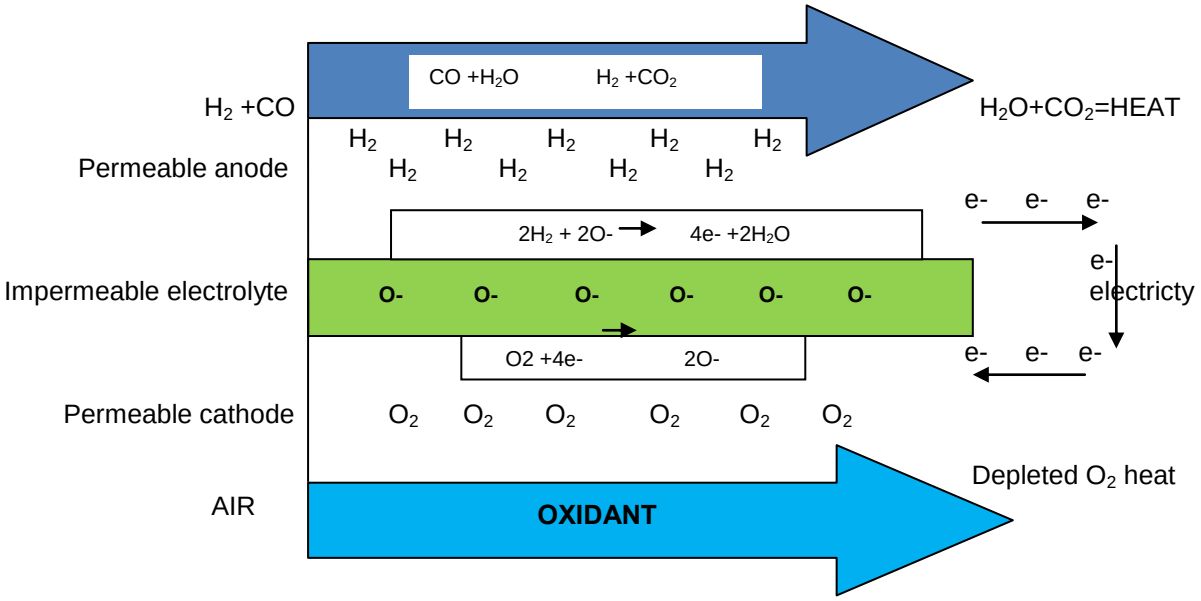

Figure 8

Model showing the processes of the solid oxide fuel cell. [35]

1.6 Aim

The aim of this study is to investigate the Brownmillerite structure with a view to introducing mixed valence manganese through controlled oxidation. This work continues initial work by Rashid[36], a former member of the group. The structures which are of interest have been studied extensively for MR and this will also be used as a foundation for my research. This study will aim to characterise the structures and space groups of the Brownmillerite phases of interest by a range of techniques, including neutron diffraction, X-ray diffraction and thermogravimetric analysis.

Sr_2MnGaO_5 and Ca_2MnGaO_5 have been previously studied, while phases containing mixture of the two A cations, strontium and calcium, have not been extensively studied. The two end members of this potential solid solution show markedly different characteristics however both show antiferromagnetic interactions. In relatively mild conditions, the pure strontium material shows an oxygen uptake to a stoichiometry 5.5 (pure Mn^{4+}), whereas calcium does not show any oxidation. This study proposes to investigate the solid solution between these phases, firstly to determine the space groups adopted by $Sr_{2-x}Ca_xMnGaO_5$ as calcium is increased. Secondly it is hoped to study the oxidised samples in this solid solution region to discover if a mixed $Mn^{3+/4+}$ state can be formed in the $Sr_{2-x}Ca_xMnGaO_{5+d}$ system, such phases should exhibit interesting magnetic properties, leading to uses as magnetoresistors and possible mixed conduction leading to use as electrodes in solid oxide fuel cells.

2 Synthetic methods

The pure strontium phase was prepared via traditional ceramic methods as followed by Wright et al.[3,19] Stoichiometric amounts of pure Mn_2O_3, (99%, sigma Aldrich) $CaCO_3$ (99%, Sigma Aldrich) and Ga_2O_3 (99%, sigma Aldrich) were calculated and ground together intensely. The sample was heated in a purged furnace at 1290° C for 12 hours under nitrogen to avoid oxidation. The mixture was reground and reheated at 1300° C.

$Sr_{2-x}Ca_xMnGaO_5$ (x=0.4, 0.5, 0.6, 0.7, 0.8, 1) stoichiometries were attempted in the temperature range 1200-1220°C. Ca_2MnGaO_5 was heated at 1170°C. Higher temperatures were used with the higher strontium content. All samples were heated twice with a slightly higher temperature for the second heating and this increased temperature was used to enhance the crystallinity. Thermogravimetric analysis (TGA) was carried out on all the samples to measure the uptake of oxygen at high temperatures.

2.1 X-ray Diffraction

X-ray Diffraction **(**XRD) is one of the most commonly used techniques to determine structural detail for solid state chemists. The wavelengths of X-rays are around 1-2 Å which is around the same length scale as the spacing between atoms in crystalline solids. Crystalline is the term used when atoms form a regular arrangement, which can be viewed as planes of atoms. Crystals may therefore be viewed as the planes of atoms stacked on top of each other to form the ordered structure. These planes are separated by a gap commonly known as their "d-spacing" and X-rays, which show wave phenomena, can be diffracted by these planes in a techniques known as X-ray diffraction.[37]

Powder XRD data were collected on the siemens D5000 and D5005 diffractometers. They both provide $CuK\alpha_1$ radiation and λ=1.5406 Å. A germanium monochromator is used with a position sensitive detector.

The waves of X-rays are diffracted by the planes of atoms as they travel through a material, this corresponds to the d-spacings present in a solid. The simplest way to view diffraction is to consider two consecutive waves travelling at the same wavelength passing through two adjacent planes in a material. The two diffracted waves interfere in such way that when they overlap in phase constructive interference occurs. When they overlap out of phase they cancel each other out and cause destructive interference. X-rays are high energy radiation typically 10keV and are able to penetrate thousands of Å into the solid before they are absorbed. The more electron density present in a material, the lower the penetration of the X-rays. As they interact with the electrons the X-rays are diffracted from the planes at a particular angle of 2theta as given by the Bragg equation.

Two X-rays of the same wavelength land on two adjacent planes in the crystal at points D and B respectively, a schematic diagram is shown in **figure 9**. The second

wave travels an extra distance AB + BC. If this extra distance is a whole number of wavelengths then the two waves are in phase and constructively interfere to produce a diffracted X-ray beam. If this distance is not a whole number of wavelengths then destructive interference occurs and no X-ray beam is produced. The path difference travelled by the two waves is formulated to be 2dsinθ which gives us the Bragg law.

Eq.2 AB (or BC) = dsinθ, which gives nλ = 2dsinθ

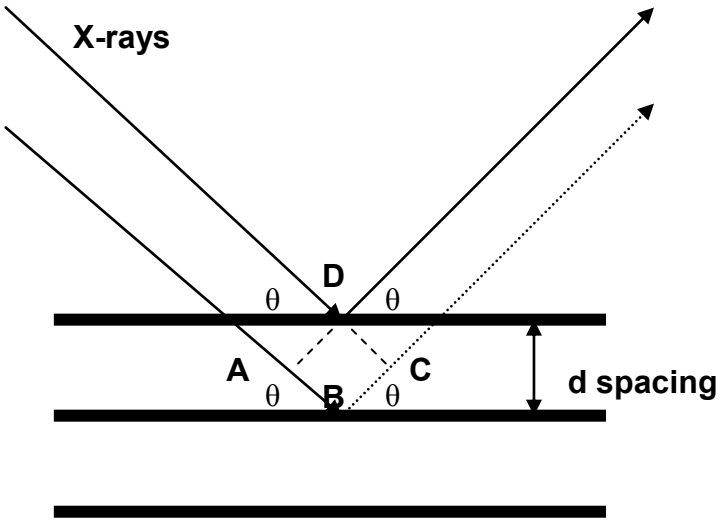

Figure 9

Schematic diagram showing the lattice planes in a crystalline solid, which show diffraction in a parallel constructive manner

This process is repeated for thousands of lattice planes and counts of intensity are measured at a chosen angle range. A significant amount of electron interaction at a particular angle represents the high intensity peak shown in the diffraction pattern. Crystal lattice planes are labelled by miller indices (h, k and l). The detector moves through a range of θ and detects reflections possible from the different lattice planes

in the solid. The position and intensity of these reflections are distinctive to its crystal structure. [38]

Crystalline solids are made up of regular repeating blocks called unit cells which are divided into seven crystal systems. Each unit cell has 6 parameters to describe the dimensions; *a, b* and *c* to describe the lengths in the x, y and z direction and *α, β* and *γ* which correspond to the angles between *a, b* and *c*. The crystal structure that will be studied in this work is orthorhombic, which possesses different values for *a, b* and *c* and 90° for all angles (*α, β* and *γ*).

2.2 Rietveld Refinements

This is a technique first developed by Hugo Rietveld in the 1960s[39]. This procedure obtains a least-squares fit between the calculated and observed intensities measured at equal angular intervals on powder XRD or neutron powder data. Manipulation of the model used to produce the calculated data allows a number of parameters to be varied and optimised. These include both structural parameters (e.g. atomic positions, lattice parameters) and instrumental parameters (e.g. peak shape, background). By minimising the differences between the calculated model and the actual data, important structural information may be obtained.

Rietveld refinement provides a solution to the problem of overlapping peaks that is commonly found in XRD plots and had previously limited its analysis. The separation of those overlapping peaks into their individual components allows an accurate structure to be determined.

The Rietveld program used in this study to analyse data was the General Structural Analysis System (GSAS).[38] The main parameters used to analyse progress of the refinement (i.e. the goodness of fit) were R_p, R_{wp}, R_e and χ^2. These are shown in Equations 3-6.

Eq.3 $$R_P = \frac{\Sigma y_i(obs) - y\ (calc)}{\Sigma y_i(obs)}$$

Eq.4 $$R_{wp} = \left[\frac{\Sigma w_i (y_i(obs) - y_i(calc))^2}{\Sigma w_i (y_i(obs))^2}\right]^{1/2}$$

Eq.5 $$\chi^2 = \left(\frac{R_{wp}}{R_e}\right)^2$$

Eq.6 $$R_e = \left[\frac{(n-p)}{\sum w_i (y_i(obs))^2}\right]^{\frac{1}{2}}$$

R_p is the sum of the differences between the observed and calculated points. R_{wp} is similar to that of R_p however, R_{wp} is more accurate as it involves the weighted profile which gives more weight to the differences in peak intensity rather than the background. The value χ^2 is also used as a guide to the goodness of fit. The lower this value the better the fit. This is the statistical comparison between the actual fit and a theoretical fit; R_e. *n* is the number of data points in the profile and *p* is the number of variables. The minimum value that can be achieved is 1.

The model is refined in a way to allow for the best fit to be achieved. This process is continued until the best fit is satisfactory. It must also be noted that there has to be a chemical feasibility to the resulting model as the program will purely search for the best fit to the data.

Statistical parameters can also be misleading. A small χ^2 may result from an incorrect structure displaying little physical and chemical sense. Similarly a large χ^2 does not necessarily mean that the model was absolutely inaccurate. For these reasons it is important to consider not only statistical measures of fit but also study the actual data by eye and consider the structural parameters generated.

Below is shown the order and directions of programs used in GSAS. Raw data is first converted to a DAT format readable by GSAS.

Step1

Raw Data file
Obtained from Diffractometer

Step2

CONVX
Converts raw data into DAT format which is readable by PC GSAS

An experimental (EXP) file is the file containing information about the model which will be used, including the specific space group. A PRM file is the file containing specific information about the diffractometer which was used to collect the data. Both of these files along with the DAT file are needed to start the refinement.

Step 3

GSAS: EXPEDT
After selecting the Experimental name, this dialogue controls all the refinement aspects.

Step 4

POWPREF
This prepares the profile for least squares refinement.

Step 5

GENLES
This dialogue carries out the refinement than generates a new updated EXP file.

POWPLOT dialogue is then used to plot the diffraction pattern which shows the two datasets, theoretical and actual, and also shows the difference curve. The LST dialogue can be viewed to learn the results of the refinement and has the history of all the refinements carried out in the EXP file. DISAGLE is used to generate the angles and bond lengths in the unit cell. PUBTABLES will then generate a table listing the important factors for publishing purposes. [39]

2.3 Thermogravimetric Analysis (TGA)

TGA is an experimental technique by which a sample can be heated, often in a controlled atmosphere, whilst the mass and energy changes are being monitored. In this work, the oxidation of samples was monitored whilst they were heated in air. Any measured weight increases were assigned the take up of oxygen. Using the formula: No. of moles = Mass / Molecular Formula, the stoichiometry of oxygen in the final oxidised material can be worked out. TGA was carried out using two different instruments. The first is the Rheometric STA 1500 thermal analyser, the second is an older Stanton Redcroft analyser. The newer TGA provided electronic data, whereas the older instrument produced data on a chart recorder. The older TGA was used initially when access to the new instrument was limited. The two different methods of collection are comparable.

2.4 Magnetic Measurement (PPMS)

A Quantum Design Physical Properties Measuring System (PPMS) was used to measure the magnetic susceptibility of the materials produced during this study. The PPMS can expose samples to variable temperatures (2-400K) and magnetic fields (0-7 Tesla) and has been designed to perform a range of experiments. It consists of a sealed chamber with 2.6 cm sample access. It is self contained with a microprocessor controlled device. The continuous low temperature control maintains the temperature below 4.2 K for long periods and has smooth transitions when warming and cooling through the temperature range. The AC magnetometry system

provides the excitation field for AC measurements, while the detection coils measure the samples magnetic response. [40]

A Quantum Design SQUID magnetometer (School of Physics) was also used to measure magnetic susceptibilities in this report. This is the superconducting quantum design interference device which is made up by combining two superconductors separated by a thin oxide barrier, acting as a weak insulator. This is known as the Josephson junction. The sensitivity of the squid allows for the measurement of very weak signals.

2.5 Neutron Powder Diffraction

Using NPD is more advantageous than XRD for analysis of lighter elements like oxygen. Lighter atoms are visible to neutrons despite the presence of heavier atoms and neighbouring atoms in the periodic table can be distinguished from each other. Neutron data can give us more information about the arrangement of these atoms and of the ordered or disordered arrangement of the oxygen's. This is particularly important in this work where small changes in oxygen positions lead to different space groups.

NPD can reveal information that cannot be seen by other radiation. Neutrons are non destructive and can travel deep into condensed matter which makes them ideal for study of samples under extreme pressure, temperature, magnetic fields and inside reaction vessels.

NPD is a crystallographic method for the characterisation of the magnetic order and structure of a material. A highly collimated beam of thermal or cold neutrons are bombarded at the sample. The neutrons are deflected by the atoms as they interact with the nuclei of the atoms, which undergo elastic collision. At the spallation source at ISIS, RAL, the time it takes for the neutrons to travel a certain distance is measured; this is known as the time of flight. Time of flight technique is used to

differentiate the energies of the incident neutron, therefore a monochromator is not needed. Time of flight can then be converted to the d-spacing. Neutron diffractometers are equipped with liquid helium cooling systems for samples so that data can be collected as low as 4.2 K.

Neutrons are found in the atomic nucleus of all atoms, however they are bound in the nucleus and do not contribute greatly to chemical reactions. The technique requires free neutrons and as they have a short half life they do not occur in nature spontaneously. Neutrons can be set free through nuclear decay or nuclear fission in a reactor (e.g. ILL in Grenoble, France) or at spallation sources (e.g. ISIS at RAL) where a heavy metal target is bombarded with high energy protons. Neutron wavelengths range from 0.1 Å to 1000 Å which makes it ideal probing structures in this study. The energies of neutrons are the same as mobile atoms in solids and liquids; they are also similar to that of atoms in single crystals and vibrational modes in molecules.

In this work, NPD was carried out in the Rutherford Appleton laboratory (RAL) in Oxford and also in the ILL facilities in Grenoble, France. At RAL, my team and I worked on the ISIS Polaris diffractometer.

At ISIS the neutrons were produced by the spallation process. A heavy metal target is bombarded with pulses of very energetic protons from a very powerful accelerator, thus colliding with the nuclei of the target atoms. This results in intense neutron pulse. The spallation target is made from the heavy metal tantalum. Protons hit the nuclei in the target material which causes it to trigger an intranuclear cascade. This excites individual nuclei to higher states which then release energy by evaporating nucleons. Some of these neutrons leave the material whereas some go on to initiate further reactions. Each high energy proton delivered to the target creates 15 neutrons.

The neutrons produced in this facility are highly energetic and can be slowed down for useful experimental conditions. This can be possible using small hydrogenous moderators around the target. The large scattering cross section of hydrogen slows down the neutrons passing through from the repeated collisions with the hydrogen nuclei. The neutrons in the pulsed source are produced in a different way to those produced in a continuous nuclear reactor. In particular is the adoption of the time of flight technique; This is used on the polychromatic neutron beam which gives a direct determination of the energy and wavelength of each neutron and allows for a fixed scattering geometry to be used.

Neutrons possess a magnetic dipole moment which makes them sensitive to magnetic fields. Neutrons are uncharged however they carry a spin and so they interact with magnetic moments and electron clouds around an atom. Neutron diffraction can give information on the microscopic magnetic structure of the material. The scattering power of a neutron off an atomic nucleus depends on the orientation of the neutron and the spin of the atomic nuclei in the target sample.

The Polaris diffractometer used at RAL has 5 detector banks. They are situated at different angles of; 35, 90, 145 and 180 degrees. The bank which is most useful with respect to the samples being studied is the C bank which has an elevation of 145 degrees. Most of the neutrons will be scattered towards the C bank. The 35 degrees bank known as the A bank, will detect the backscattered deflections of neutrons. These will be most useful for the low temperature magnetic peaks which will appear in this region.[30]

3 Results and Discussion

3.1 Synthesis and initial characterisation

The synthesis of samples of stoichiometry $Sr_{2-x}Ca_xMnGaO_5$ (X=0, 0.4, 0.5, 0.6, 0.65, 0.7, 0.8, 1 and 2) was attempted and short XRD datasets were collected on all samples to determine initial sample purity. With this initial sample purity confirmed, long overnight scans were taken, collecting over a 2θ range of 5-90° for 10 hours. A more detailed assessment of purity was then possible and lattice parameters were calculated. The overnight X-ray diffraction scans are shown in **figure 10**.

Analysis of these scans showed that the samples were effectively single phase and peaks were shifted towards the right, which is to higher 2theta, as strontium content was lowered. This indicated that the d-spacing of reflections was decreasing, and this was quantified by unit cell calculations.

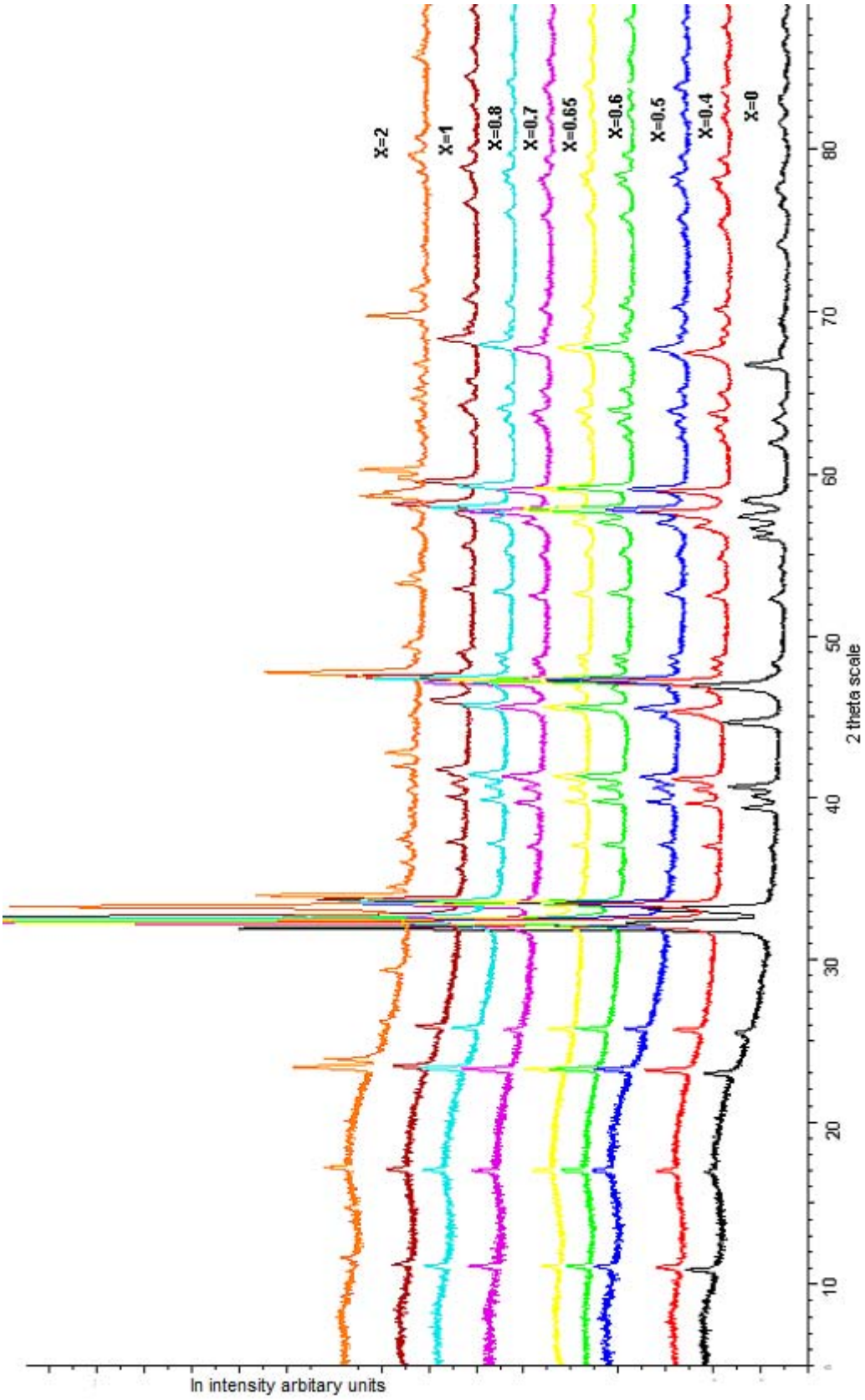

Figure 10
X-ray scans of the stoichiometric range $Sr_{2-x}Ca_xMnGaO_5$ (x= 0, 0.4, 0.5, 0.6, 0.65, 0.7, 0.8, 1 and 2)

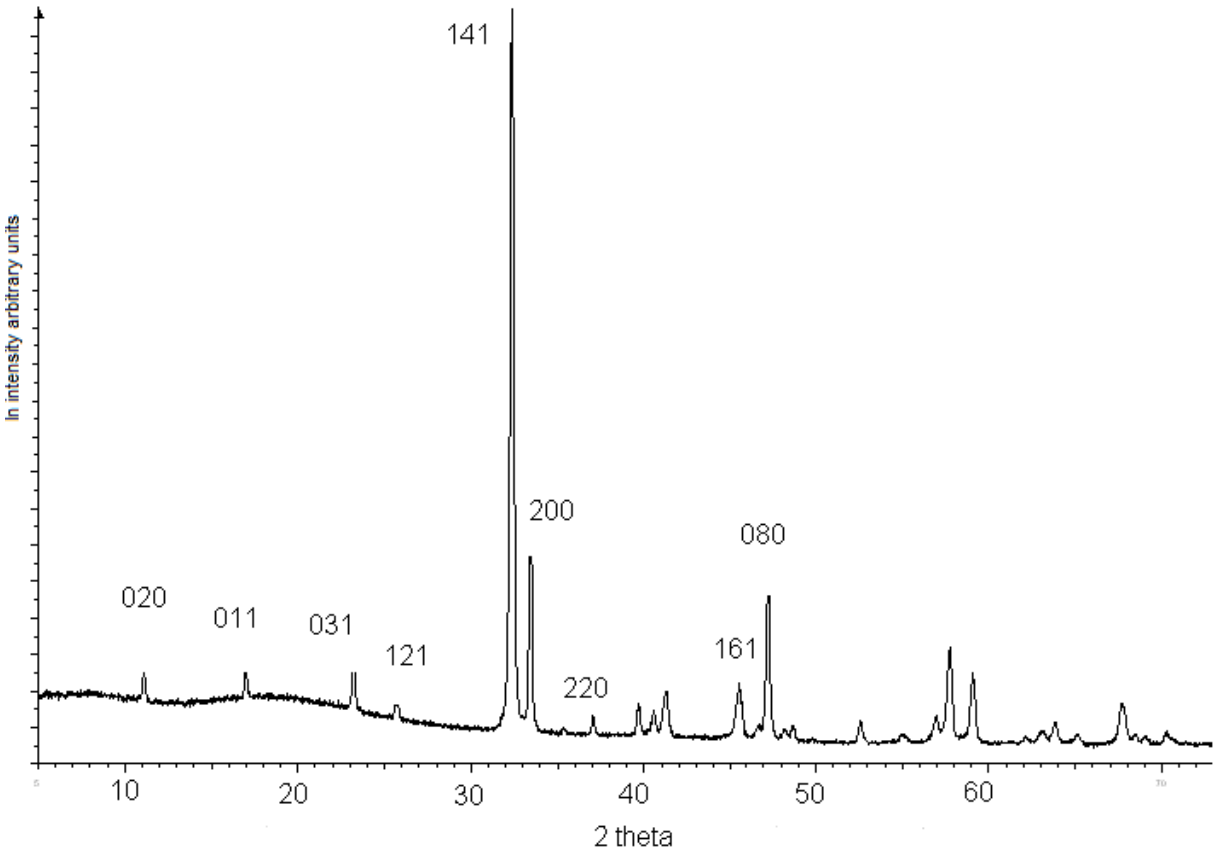

Figure 11
XRD peaks assigned with their specific *hkl* reflections
of $Sr_{1.4}Ca_{0.6}MnGaO_5$

3.2 Unit Cell Size

From further analysis of XRD scans, d-spacing values were determined and peaks were assigned to appropriate *hkl* reflections as shown in **figure 11**. This was achieved with the aid of the program DSPACE, which generated *hkl* values for d-spacings from a given unit cell and space group. Once the observed d-space values were matched with the potential *hkl* values the CELL program was used to determine the unit cell using least squares minimisation.

The obtained unit cell parameters are shown in **table 1**. A plot of lattice parameters with changing calcium content is shown in **figure 12**. It is clear from this that *a, b* and *c* decreased on going from the pure strontium phase to the pure calcium phase. This is a consequence of replacing strontium with the smaller calcium in the structure. The unit cell tends to be more compact with the higher calcium content and this can be linked to the increased order of the GaO_4 chains. [8]

There is no obvious difference in the behaviour of the lattice parameter with changing strontium content and therefore the change in unit cell size appears isotropic. Error bars have not been include as they were considerably small and not visible.

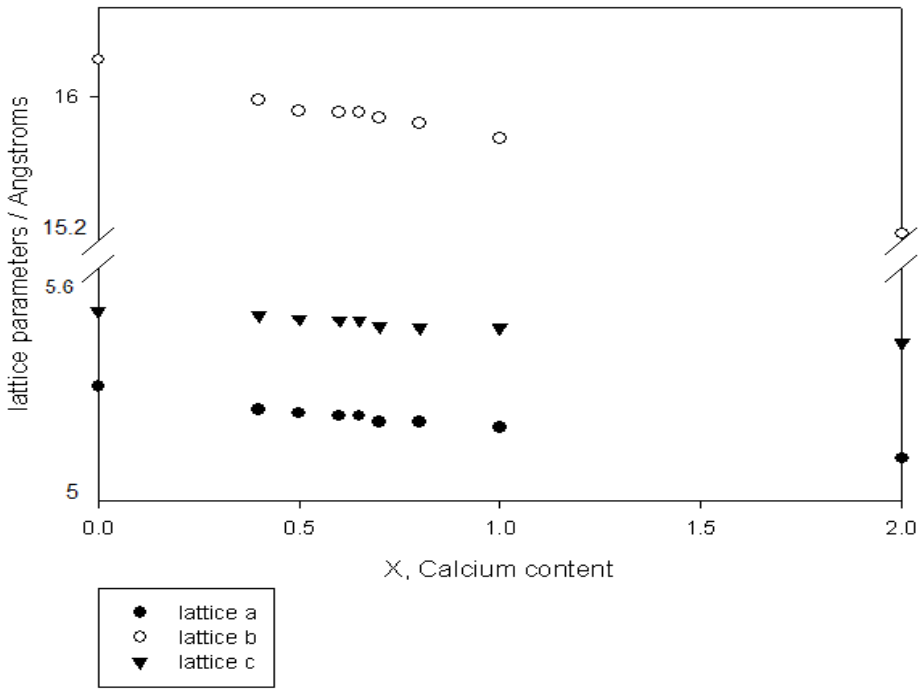

Figure 12

Lattice parameters of $Sr_{2-x}Ca_xMnGaO_5$.

Table 1

Table of lattice parameters

$Sr_{2-x}Ca_xMnGaO_5$	Parameter *a* Å	Parameter *b* Å	Parameter *c* Å
X= 2	5.273 (2)	15.237 (6)	5.471 (2)
X=1	5.326 (3)	15.768 (8)	5.497 (3)
X=0.8	5.335 (2)	15.855 (7)	5.497 (3)
X=0.7	5.336 (2)	15.884 (6)	5.501 (2)
X=0.65	5.334 (2)	15.852 (5)	5.501 (2)
X=0.6	5.341 (3)	15.903 (8)	5.507 (3)
X=0.5	5.351 (2)	15.923 (6)	5.513 (2)
X=0.4	5.356 (2)	15.983 (6)	5.519 (2)
X=0	5.396 (2)	16.211 (7)	5.525 (2)

The unit cell volume has also been plotted, **figure 13**, and this shows a similar trend with changing strontium content. The more calcium in the structure the smaller the unit cell volume, however, there were some close similarities in the unit cell volume with stoichiometries x=0.7 to x=0.6. This means that the phase formed in these samples may have the same composition, suggesting that there is a preferred composition within the solid solution range.

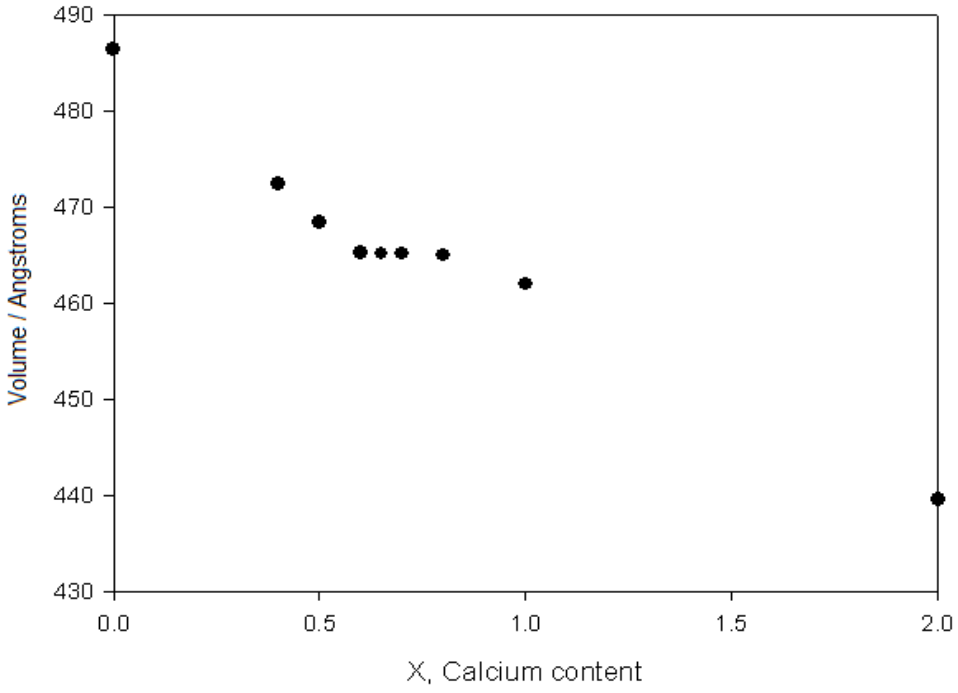

Figure 13

Volume of unit cell for $Sr_{2-X}Ca_XMnGaO_5$

3.3 Thermogravimetric Analysis

To determine the potential oxidation of samples, thermogravimetric analysis **(**TGA) was carried out on all samples synthesised. Samples were heated in the presence of oxygen and the increase in mass was assumed to be due to oxygen uptake. The following shows an example of the calculation of the oxygen content for sample $Sr_{1.5}Ca_{0.5}MnGaO_5$. From the TGA data, **figure 14**, the increase in mass was taken as the difference between the plateau, and the highest point of the mass. An initial

stoichiometry of O_5 was assumed and then a final stoichiometry could be estimated from the mass increase. This estimation, although not providing exact oxygen contents is able to provide a means of comparison of these samples oxidative behaviour.

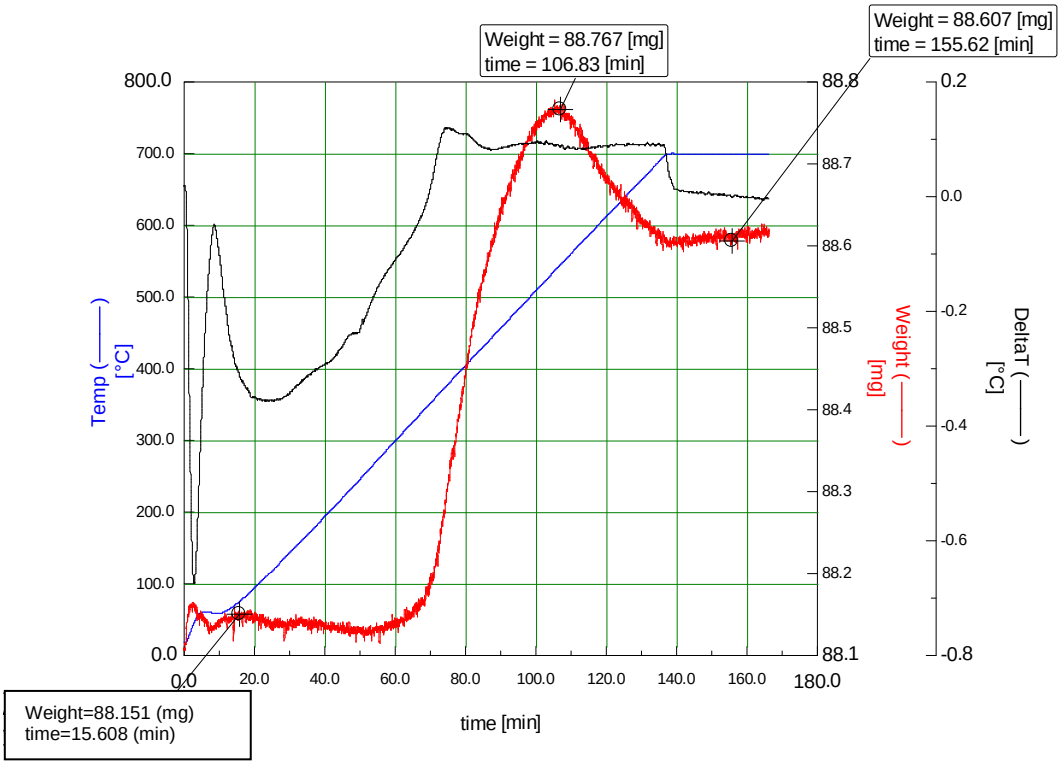

Figure 7

TGA data for $Sr_{1.5}Ca_{0.5}MnGaO_5$ using the Rheometric Thermal Analyzer 1500

The maximum uptake was found to be around 500°C in all samples and is consistent with previous reported data. **Table 2** shows the average oxygen uptake using the Rheometric thermal analyser and the Stanton Redcroft analyser. [19,20]

Table 2

Comparison of oxygen uptake

$Sr_{2-x}Ca_xMnGaO_5$	Average Oxygen uptake
X= 2	5 no uptake
X=1	5 no uptake
X=0.8	5 no uptake
X=0.7	5.07 (2)
X=0.65	5.138(5)
X=0.6	5.144(5)
X=0.5	5.175(3)
X=0.4	5.327(9)
X=0	5.422(3)

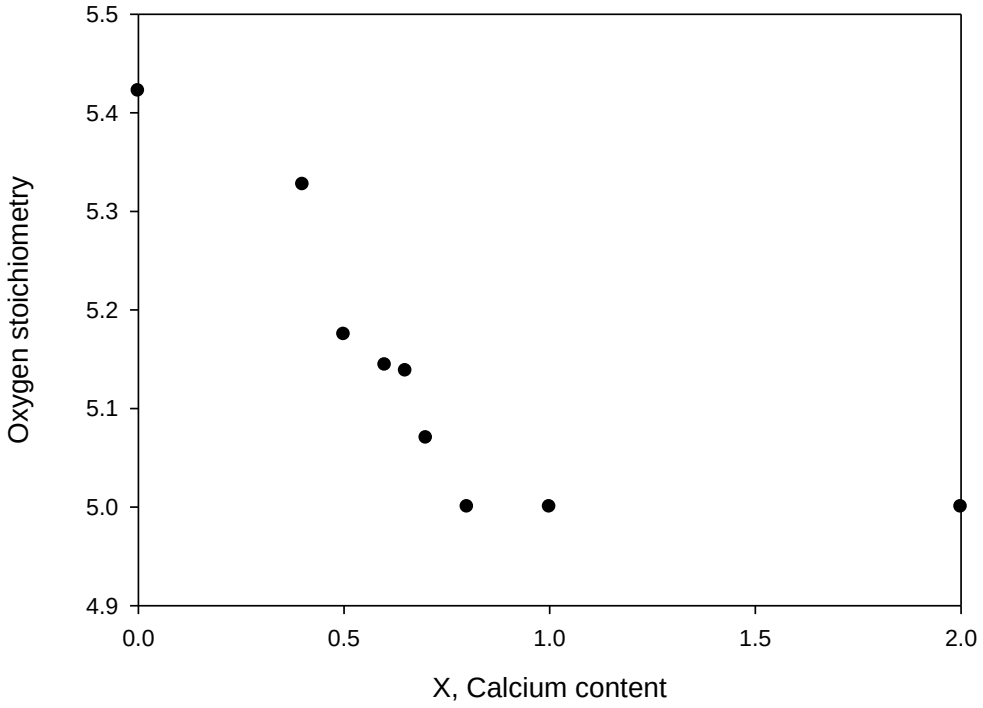

Figure 8

This graph shows oxygen uptake of the system $Sr_{(2-x)}Ca_xMnG$ Using Stanton Redcroft analyser. Error bars are not shown as they were considerably small and not visible.

These results showed that $Sr_{2-x}Ca_xMnGaO_5$ (x= 0.65-0) appeared to take up oxygen, whereas x=0.7 and above did not show any mass change (**figure 15)**. Interestingly, these results show an intermediate uptake of oxygen in the region $Sr_{2-x}Ca_xMnGaO_5$ (x=0.65-0.5) and these are potentially the most interesting samples in terms of magnetic properties and mixed conductivities. This is due to the likely mixed manganese valence $Mn^{3+/4+}$ formed by these stoichiometries. Previous reports have suggested that Ca_2MnGaO_5 and $SrCaMnGaO_5$ do not display any significant oxidation at 600°C [22] whereas Sr_2MnGaO_5 is reported to form $Sr_2MnGaO_{5.5}$ with pure Mn^{4+}.[24] It may be speculated that the phases containing higher Ca content, which possess a more ordered structure, as demonstrated by their space groups, are less

able to be oxidised because of the increased stability of their more compact GaO layers.

The XRD pattern of an oxidised material with x=0.6 is compared to the original "as-synthesised" sample in **figure 16**. In the oxidised scan there appears to be an extra peak (circled) in between the two major peaks which suggests there are changes in the sample after oxidation. All peaks appear to shift to higher 2theta by very small amounts. This suggests that none of the original "as-synthesised" sample remains, however it was not possible to index the resulting pattern and it was not clear if this oxidised product was a single phase.

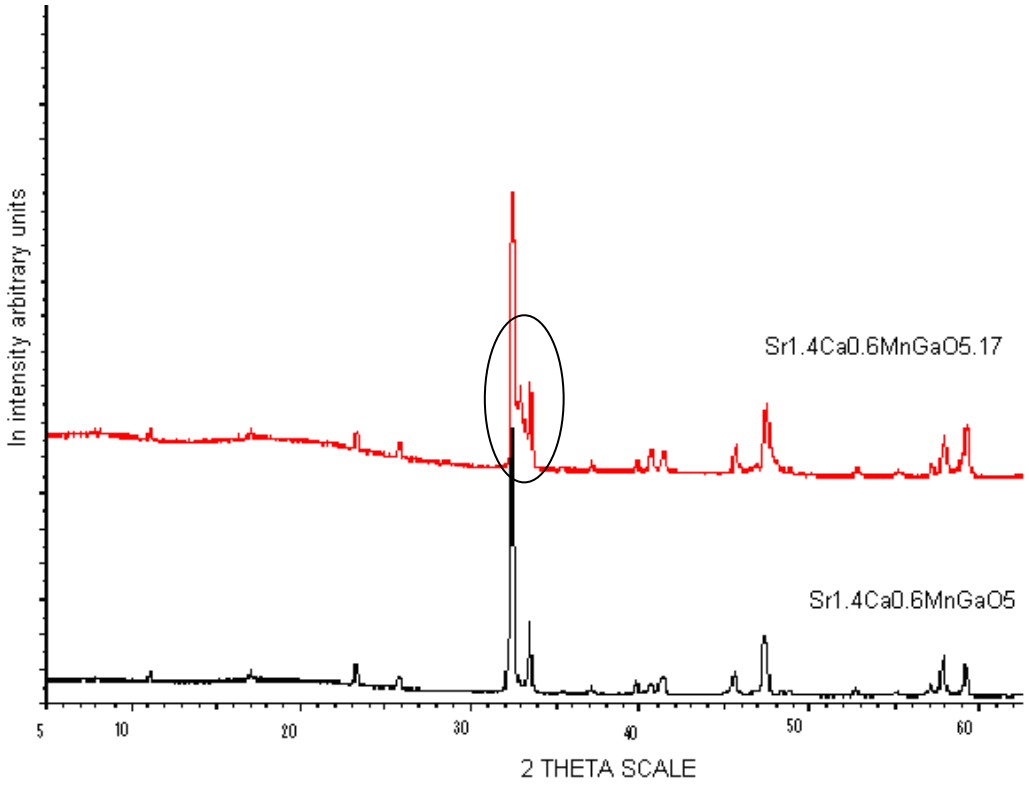

Figure 9
XRD scan showing the oxidised material (red)
and the original 'as synthesised' sample (black)

From TGA data, Sr_2MnGaO_5 is oxidised to oxygen stoichiometry of around 5.42 and certainly not to 6, which would equate to an otherwise stoichiometric perovskite structure (ABO_3). It would therefore appear that the Mn^{4+} is the stable oxidation state and a higher oxidation state is energetically unfavourable. This observation would appear to indicate that the driving force for the oxygen uptake is to fully oxidise Mn^{3+} to Mn^{4+} and not to fill available oxygen sites. In contrast, $SrCaMnGaO_5$ has not displayed the same inclination to oxidise its Mn^{3+} and so the structure must be prohibiting this process. $Sr_{1.5}Ca_{0.5}MnGaO_5$ was shown to take up oxygen up to $Sr_{1.5}Ca_{0.5}MnGaO_{5.19}$ apparently creating some Mn^{3+} and some Mn^{4+}. Mixed manganese valence could give rise to potentially magnetoresistant properties, mixed conductivities and it should be ferromagnetic, similar to that of the structure $(La,Ca)MnO_3$ which has comparable properties. The mixed manganese valence appear to be formed in the stoichiometry $Sr_{2-x}Ca_xMnGaO_5$, (X=0.5-0.65).

3.4 Magnetisation

Magnetic measurements were carried out on the range of $Sr_{2-x}Ca_xMnGaO_5$ (X=4-6) using a Quantum Design Physical Properties Measurement System (PPMS). The magnetization of the ‘as synthesized’ form of X=0.5 was measured and is shown in **Figure 17.** These data show the magnetization in field coolled and a zero field coolled conditions with a Neel temperature of 162 K.

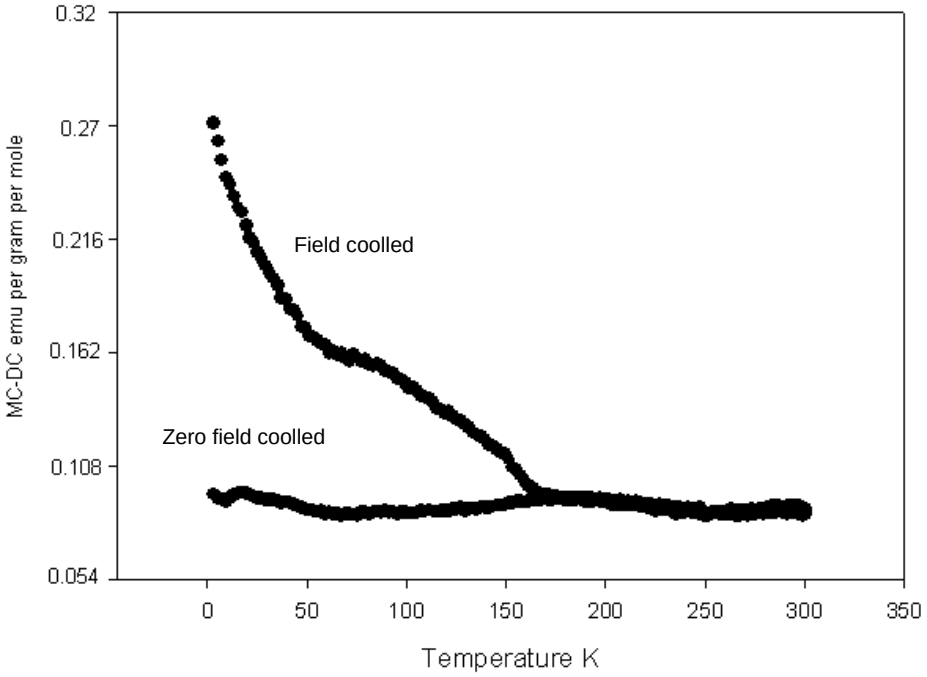

Figure 10

Field coolled and zero field coolled data are shown for $Sr_{1.5}Ca_{0.5}MnGaO_5$ as synthesized. As the field is applied, the magnetisation starts to increase gradually at 162K.

The data presented is of $Sr_{1.5}Ca_{0.5}MnGaO_5$ 'as synthesized' and shows typical features of a material displaying canted antiferromagnetism. This occurs when the moments align in an antiferromagnetic manner but are not completely co-linear. Therefore a resultant moment occurs and there is a difference between field coolled and zero field coolled data. A similar behaviour is also observed for $SrCaMnGaO_5$ which is thought to have the same space group with a Neel temperature of 159 K which compares closely with these results.[22] The pure strontium phase does not however show the same canted arrangement and it also shows a different space group to those previously mentioned. An oxidised form of $Sr_{1.5}Ca_{0.5}MnGaO_5$ was also measured, however did not show any ferromagnetic component, just paramagnetism. This is surprising since we may have expected that the intermediate oxygen content would provide mixed valent Mn, and potential for ferromagnetic behaviour. Clearly

the oxidation has disrupted the canted antiferromagnetic order but has not led to ferromagnetic order.

3.5 Neutron Diffraction Results

To further investigate the intermediate oxygen uptake stoichiometry, neutron data were collected on samples $Sr_{2-x}Ca_xMnGaO_5$ x=0.7, 0.65, 0.6, 0.5. Each were analysed at room temperature and low temperature. **Table 3** lists all the data sets collected using neutron diffraction. Each as synthesized data set was analysed using the three different space groups possible for Brownmillerite phases to identify the preferred space group for each stoichiometry. This was assigned based on the best fit to the given data. [2, 8]

Table 3
Table of chi^2 values from analyses performed on data at 300 K

$Sr_{2-x}Ca_xMnGaO_5$	X= 0.7	X= 0.65	X= 0.6	X= 0.5
Ibm2	*7.83*	*12.35*	*13.52*	*13.58*
Icmm	-	*29.19*	*27.12*	*22.19*
Pcmn	-	*44.24*	*41.39*	*33.91*

From these chi^2 values the lowest value was found to be that modelled with the space group *Ibm2* for all of these compositions so therefore this space group was used for all as synthesized samples studied in this report. The low temperature data were also all analysed using *Ibm2*

$Sr_{1.3}Ca_{0.7}MnGaO_5$ 'as synthesized'

Room Temperature 300 K

This set of data was collected on the D2B diffactometer at the ILL facilities in Grenoble, France. Here the data collected was from one collective bank which collected low to high angle scattering. The data were analysed by Rietveld refinement using models based on space group *Ibm2*. The Ca:Sr ratio was fixed to the stoichiometry expected. A good fit was obtained and is shown in **figure 18**. The refined parameters are given in **table 4**. Bond lengths and angles are given in **tables 12** and **13**.

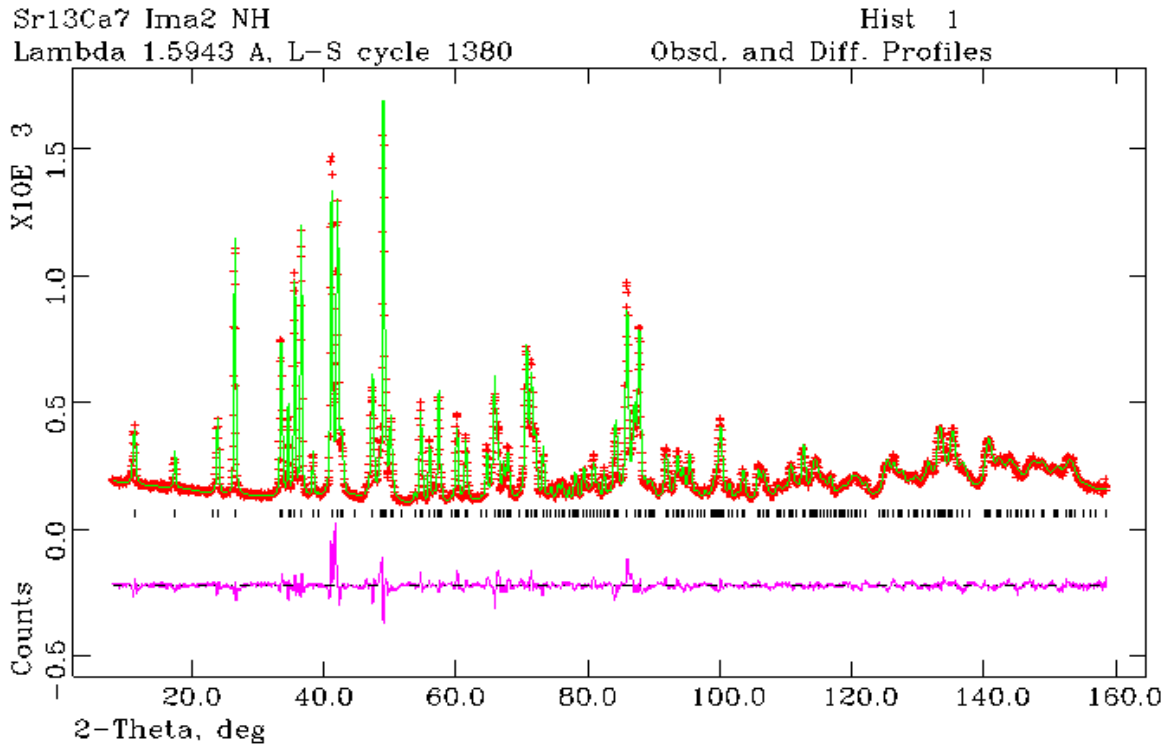

Figure 11

Rietveld profile of $Sr_{1.3}Ca_{0.7}MnGaO_5$

using NPD data in space group *Ibm2.* Observed data as crosses,

line showing calculated and difference data.

Table 4

Refined structure of $Sr_{1.3}Ca_{0.7}MnGaO_5$ from NPD data.

Atom	X	Y	Z	Ui/Ue*100	Site	Mult	Fraction (fixed)
Sr	0.112(5)	0.516(5)	0.013(8)	1.25(7)	1	8	0.6500
Mn	0.000	0.000	0.000	1.38(4)	2(001)	4	1
Ga	0.250	0.073(6)	0.053(9)	1.18(1)	M(100)	4	1
O1	0.0068(2)	0.2458(8)	0.2614(2)	0.78(6)	1	8	1
O2	0.1445(9)	-0.0502(5)	-0.0106(2)	1.33(8)	1	8	1
O3	0.250	0.3754(8)	0.8957(9)	1.38(12)	M(100)	4	1
Ca	0.1121(5)	0.5165(5)	0.0133(8)	1.25(7)	1	8	0.3500
R_{wp} = 6.17% R_P = 4.49% χ^2 = 7.830 *a* = 5.3351 (6)Å, *b* =15.8265 (8)Å, *c* =5.4977 (2) Å Volume = 464.213 (3)Å ^{3}							

$Sr_{1.35}Ca_{0.65}MnGaO_5$ 'as synthesized'

Room temperature 300 K

The following sets of data were collected in the RAL, Oxford. The data were analysed by Rietveld refinement using models based on space group *Ibm2*.The Ca:Sr ratio was fixed to the stoichiometry expected. A good fit was obtained and plotted in **figure 19**. A summary of the refined parameters are shown in **table 5**. **Figure 20** shows the expected structure of $Sr_{1.35}Ca_{0.65}MnGaO_5$ modelled on the space group *Ibm2*.

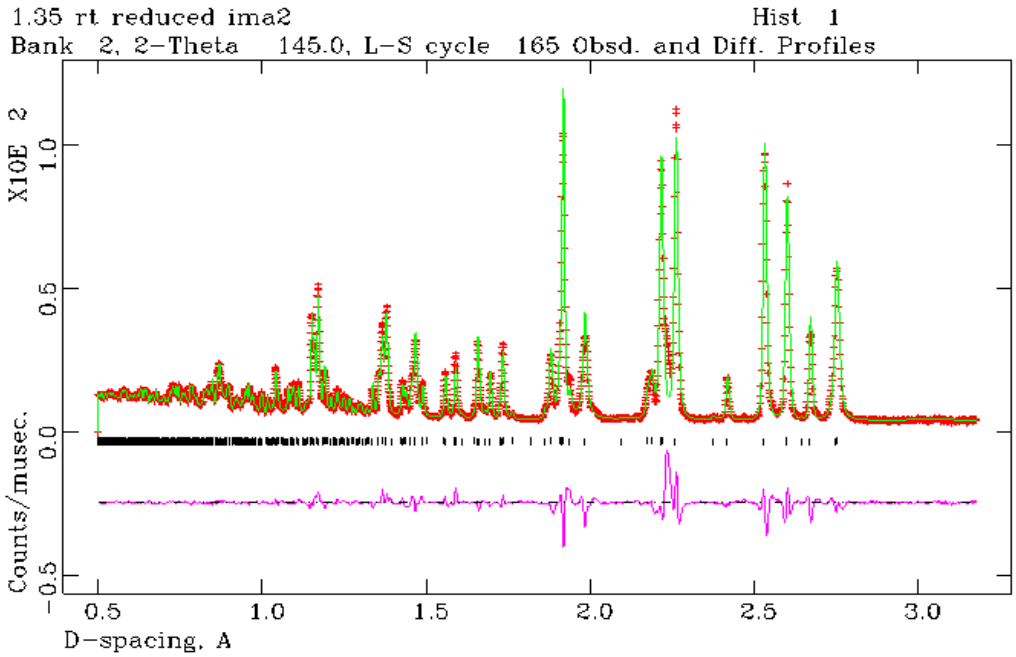

Figure 19

Rietveld profile of $Sr_{1.35}Ca_{0.7}MnGaO_5$ using NPD data in space group *Ibm2.* Observed data as crosses, line showing calculated and difference data.

Table 5

Refined structure of $Sr_{1.35}Ca_{0.65}MnGaO_5$ from NPD data

Atom	X	Y	Z	Ui/Ue*100	Site	Mult	Fraction (fixed)
Sr	0.11192(6)	0.51489(20)	0.02411(32)	0.719(20)	1	8	0.6750
Mn	0.00000	0.00000	0.0173(8)	0.65(4)	2(001)	4	1
Ga	0.25000	0.07178(4)	0.06451(3)	0.593(2)	M(100)	4	1
O1	0.00654(8)	0.24896(8)	0.2732(4)	0.401(6)	1	8	1
O2	0.14396(8)	-0.04797(9)	0.00000	0.914(3)	1	8	1
O3	0.25000	0.37611(3)	0.9093(4)	0.911(6)	M(100)	4	1
Ca	0.11192(6)	0.51489(2)	0.02411(3)	0.719(2)	1	8	0.3250
R_{wp} = 4.05% R_P = 6.61% χ^2 = 12.35 a = 5.3416(8) Å, b = 15.8613(3) Å, c = 5.5025(8) Å, Volume = 466.199 (1) Å ^{3}							

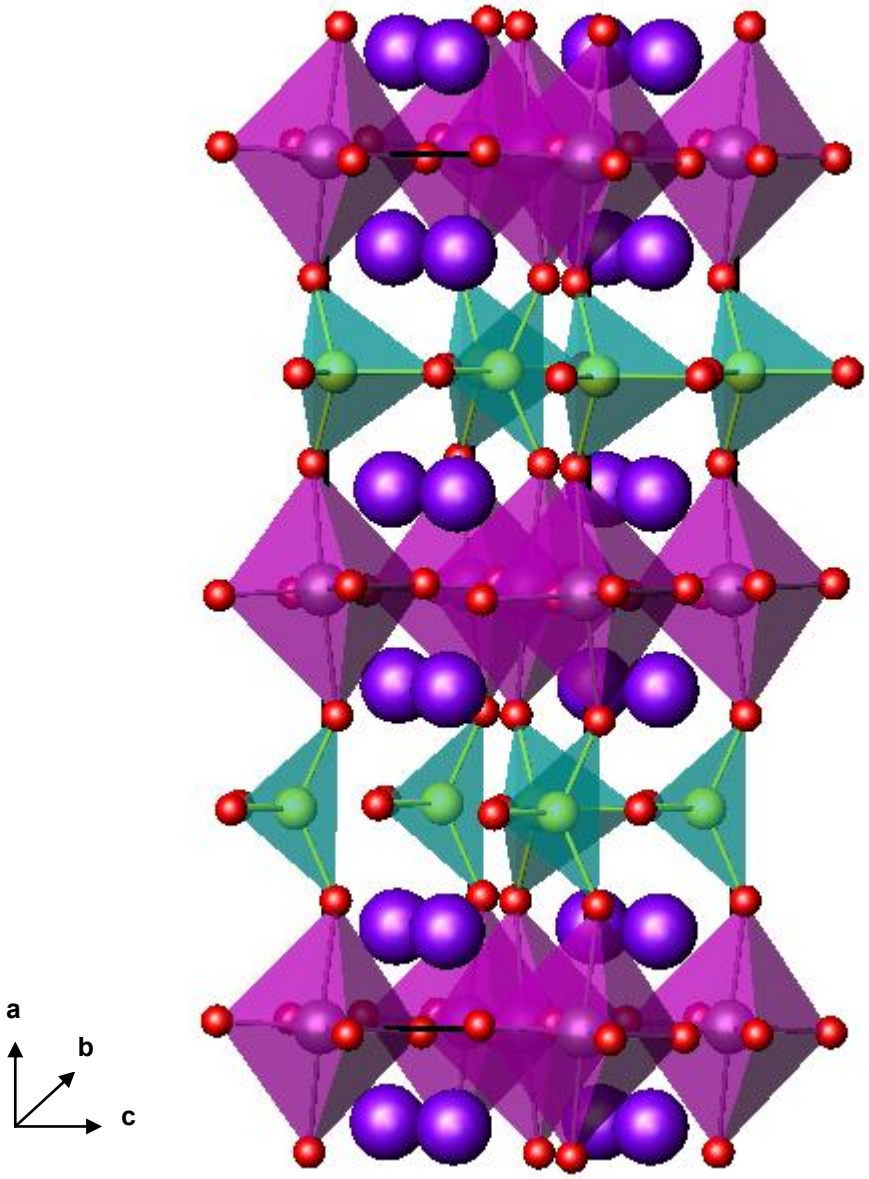

Figure 20

Structure of $Sr_{1.35}Ca_{0.65}MnGaO_5$ with the space group *Ibm2*.

octahedra=purple, tetrahedra=green, strontium/calcium=indigo

red=oxygen

$Sr_{1.4}Ca_{0.6}MnGaO_5$ 'as synthesized'

Room temperature 300 K

The following sets of data were collected in the RAL, Oxford. The data were analysed by Rietveld refinement using models based on space group *Ibm2*.The Ca:Sr ratio was fixed to the stoichiometry expected. A good fit was obtained and plotted in **figure 21**. A summary of the refined parameters are shown in **table 6**.

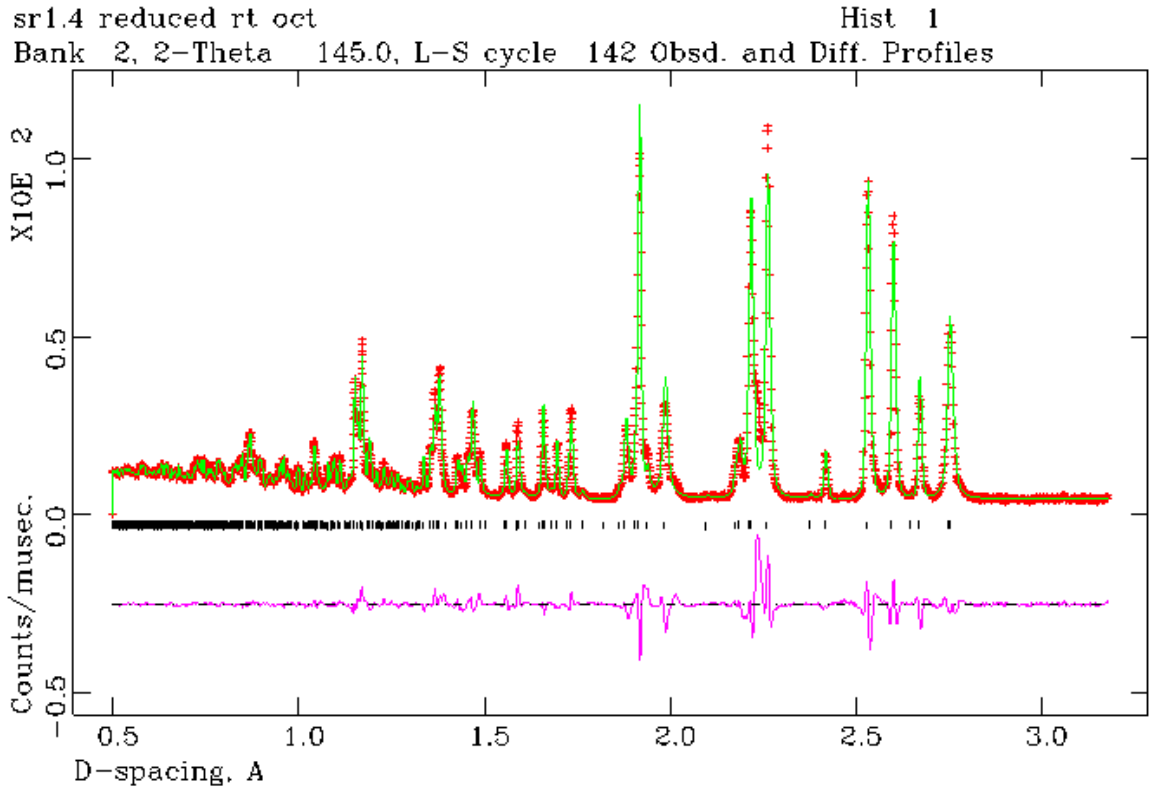

Figure 21
Rietveld profile of $Sr_{1.4}Ca_{0.6}MnGaO_5$
using NPD data in space group *Ibm2.* Observed data as crosses,
line showing calculated and difference data.

Table 6

Refined structure of $Sr_{1.4}Ca_{0.6}MnGaO_5$ from NPD data

Atom	X	Y	Z	Ui/Ue*100	Site	Mult	Fraction (fixed)
Sr	0.11210(7)	0.51473(2)	0.0230(4)	0.695(2)	1	8	0.6750
Mn	0.00000	0.00000	0.0172(9)	0.54(4)	2(001)	4	1
Ga	0.25000	0.07112(7)	0.0643(3)	0.649(2)	M(100)	4	1
O1	0.00632(9)	0.24900(3)	0.2725(4)	0.422(8)	1	8	1
O2	0.14394(9)	-0.0467(2)	0.000000	0.916(5)	1	8	1
O3	0.250000	0.37531(7)	0.9096(5)	0.937(4)	M(100)	4	1
Ca	0.11210(7)	0.51473(2)	0.0230(4)	0.695(2)	1	8	0.3250
R_{wp} = 4.40% R_P = 7.15% χ^2 = 13.52 a = 5.3424(8) Å, b = 15.8821(4) Å, c = 5.5027(9) Å Volume = 466.902 (2) Å ^{3}							

$Sr_{1.5}Ca_{0.5}MnGaO_5$ 'as synthesized'

Room temperature 300 K

The following sets of data were collected in the RAL, Oxford. The data were analysed by Rietveld refinement using models based on space group *Ibm2*. The Ca:Sr ratio was fixed to the stoichiometry expected. A good fit was obtained and plotted in **figure 22**. A summary of the refined parameters are shown in **table 7**.

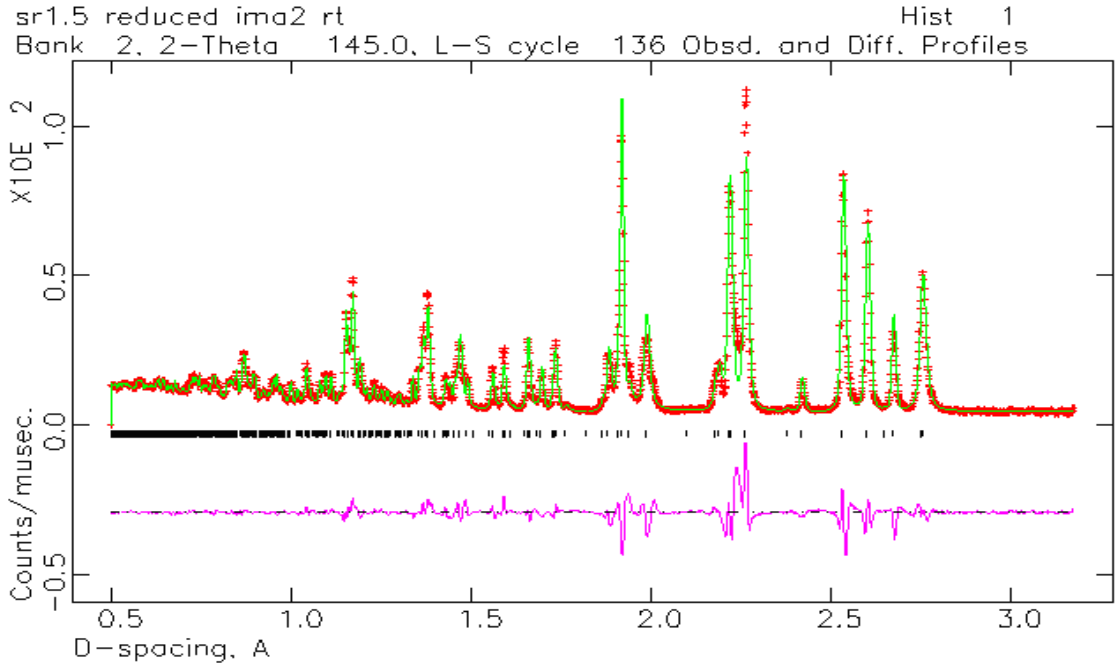

Figure 22

Rietveld profile of $Sr_{1.5}Ca_{0.5}MnGaO_5$

using NPD data in space group *Ibm2.* Observed data as crosses,

line showing calculated and difference data.

Table 7

Refined structure of $Sr_{1.5}Ca_{0.5}MnGaO_5$ from NPD data

Atom	X	Y	Z	Ui/Ue*100	Site	Mult	Fraction (fixed)
Sr	0.11241(7)	0.51395(3)	0.0220(4)	0.633(4)	1	8	0.7500
Mn	0.000000	0.000000	0.0185(1)	0.80(5)	2(001)	4	1
Ga	0.250000	0.07108(3)	0.0637(4)	0.63(4)	M(100)	4	1
O1	0.0060(1)	0.24890(9)	0.2720(5)	0.402(2)	1	8	1
O2	0.1435(1)	-0.0456(2)	0.000000	0.855(7)	1	8	1
O3	0.250000	0.37367(3)	0.9092(5)	1.020(4)	M(100)	4	1
Ca	0.11241(7)	0.51394(2)	0.0220(4)	0.633(4)	1	8	0.2500

R_{wp} = 4.59% R_P = 7.6% χ^2 = 13.58

a = 5.3510 (5) Å, b = 15.9106 (5) Å, c = 5.5097 (6) Å,

Volume = 469.092 (2) $Å^3$

Lattice parameters from neutron data were obtained and are presented in **table 8**. The parameters increase slightly with the increasing strontium content. These results are also closely comparable to the trends observed in the XRD data collected.

Table 8

Table of lattice parameters *a, b,* and *c*

$Sr_{2-x}Ca_xMnGaO_5$	Parameter *a* / Å	Parameter *b* / Å	Parameter *c* / Å
X=0.7	5.3351 (6)	15.8265 (8)	5.4977 (2)
X=0.65	5.3416 (8)	15.8613 (3)	5.5025 (8)
X=0.6	5.3424 (8)	15.8821(4)	5.5027 (9)
X=0.5	5.3510 (5)	15.9106 (5)	5.5097 (6)

3.5.1 Low temperature NPD data 4.2 K

$Sr_{1.35}Ca_{0.65}MnGaO_5$ 'as synthesized'

Extra peaks were visible in the low temperature data as compared to the room temperature data and this demonstrated the existence of magnetic order. The room temperature low angle (bank A) data is shown in **figure 23a**. The magnetic peaks are shown in **figure 23b**. These magnetic peaks were successfully modelled on space group *Ib'm2* with the manganese moments located in the z direction. The magnetic moment for $Sr_{1.35}Ca_{0.65}MnGaO_5$ was 3.199 μ_B. The space group *Ib'm2* was used for all magnetic refinements as it was shown to be the best fit for all the stoichiometries analysed. A summary of the refined parameters are shown in **table 9**.

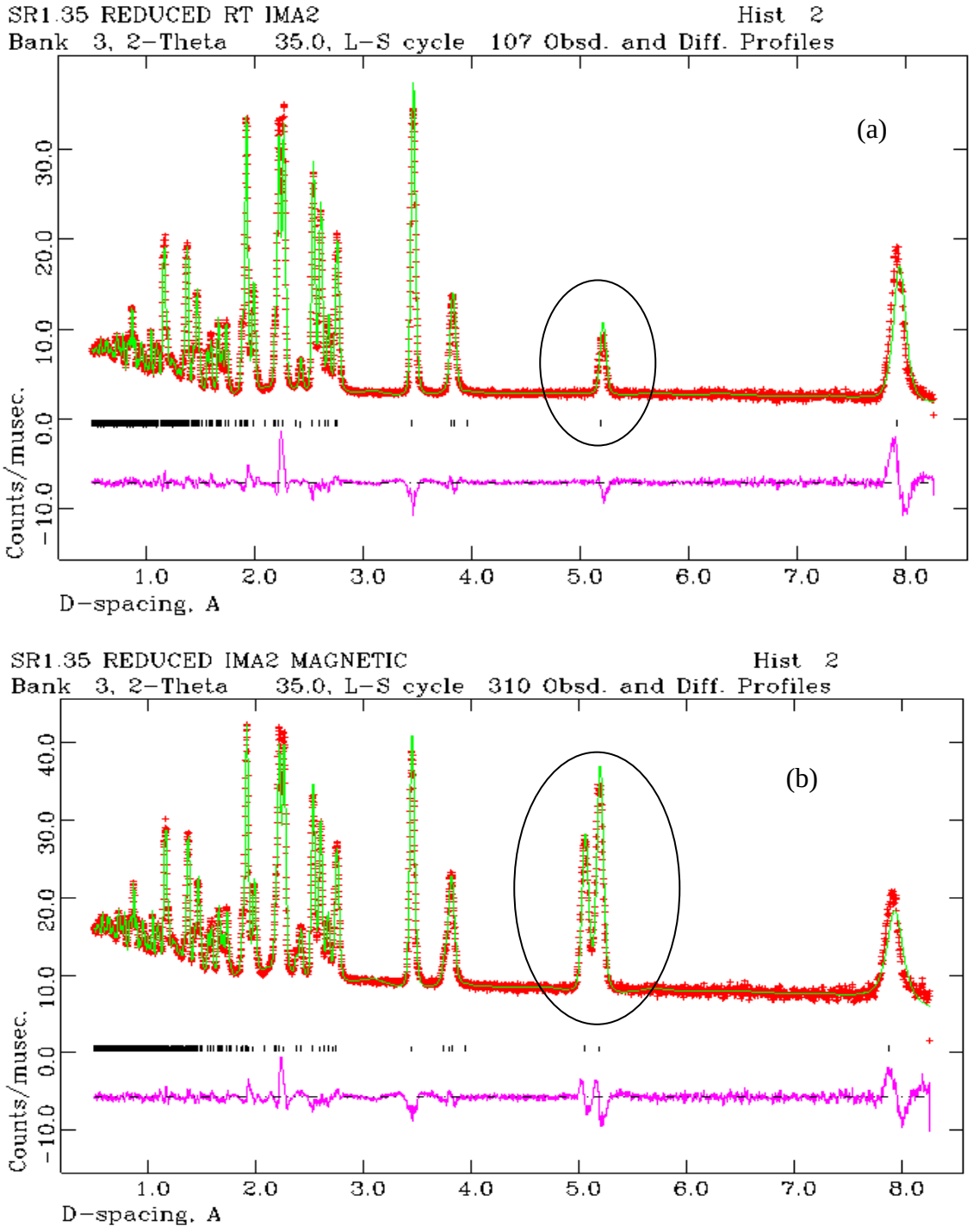

Figure 23 (a) NPD profiles for $Sr_{1.35}Ca_{0.65}MnGaO_5$ collected at room temperature peak circled at 5.2 Å D-spacing, (b) NPD data profiles for $Sr_{1.35}Ca_{0.65}MnGaO_5$ at 4.2 K with the magnetic peaks circled.

Table 9

Refined magnetic structure of $Sr_{1.35}Ca_{0.65}MnGaO_5$ from low temperature NPD data

Atom	X	Y	Z	Ui/Ue*100	Site	Mult	Fraction (fixed)
Sr	0.11182(6)	0.51533(2)	0.02448(3)	0.286(2)	1	8	0.6750
Mn	0.000000	0.000000	0.0169(7)	0.32(4)	2(001)	4	1
Ga	0.250000	0.07206(5)	0.06554(3)	0.215(27)	M(100)	4	1
O1	0.00649(9)	0.24905(4)	0.2741(4)	0.106(16)	1	8	1
O2	0.14413(8)	-0.0479(9)	0.000000	0.428(21)	1	8	1
O3	0.2500	0.37654(5)	0.9114(4)	0.522(35)	M(100)	4	1
Ca	0.11182(6)	0.51533(2)	0.02448(3)	0.286(20)	1	8	0.3250
R_{wp} = 2.35% R_P = 3.89% χ^2 = 9.285 *a* = 5.3274(8) Å, *b* = 15.8440(4) Å, *c* = 5.48998(9) Å Cell Volume = 463.400 (2) Å ^{3}							

$Sr_{1.4}Ca_{0.6}MnGaO_5$ 'as synthesized'

Low temperature 4.2 K

Figure 24a shows the room temperature bank A data where the room temperature peak is circled. In **figure 24b** the magnetic peaks which have been circled can be seen at 4.2 K. The refinement of these data was performed in a similar way to the previous section using magnetic space group *Ib'm2* in with the moment in the z direction. **Table 10** shows the refined parameters.

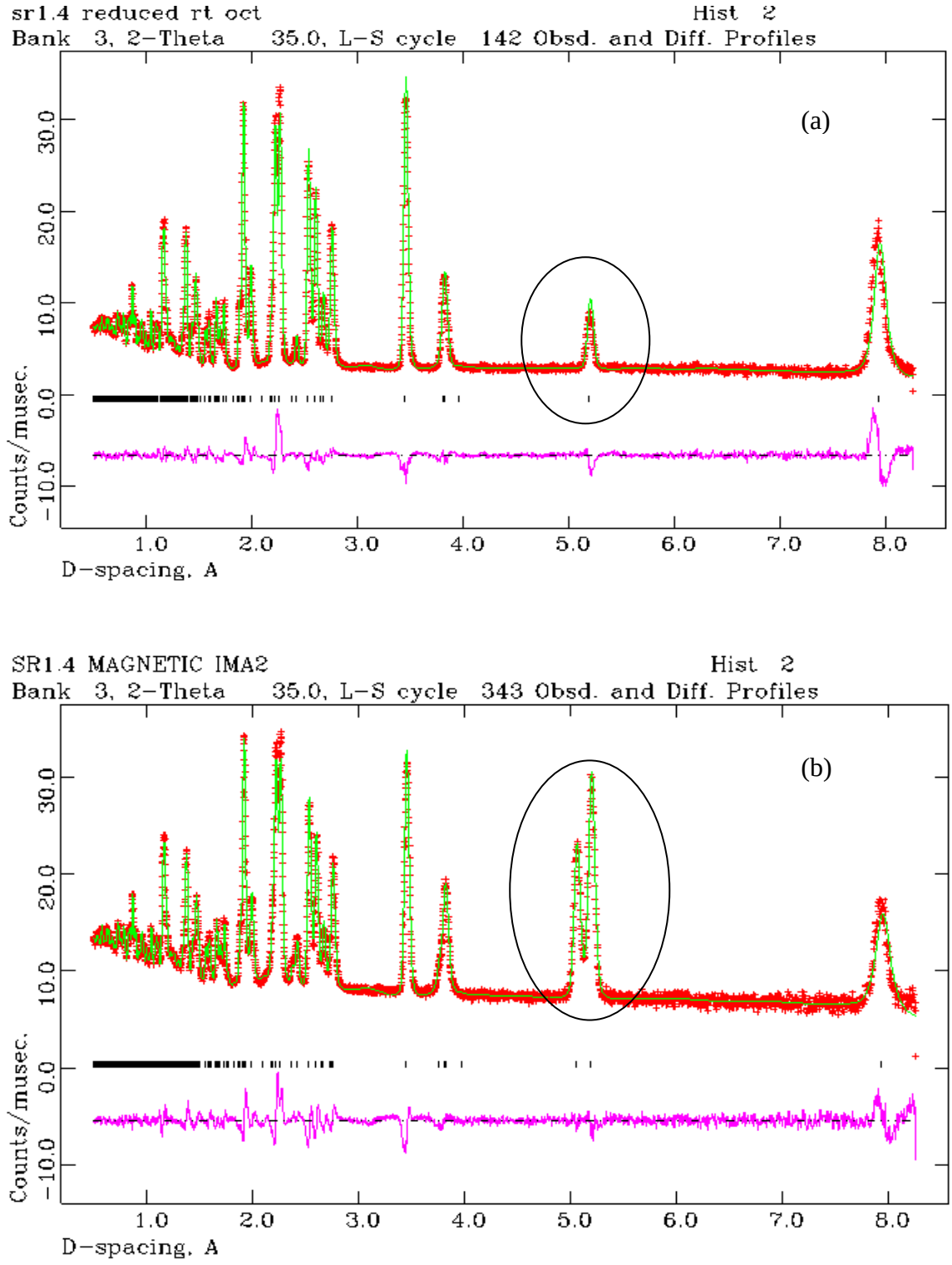

Figure 24 (a) NPD profiles for $Sr_{1.4}Ca_{0.6}MnGaO_5$ collected at room temperature peak circled at 5.2 Å D-spacing, (b) NPD data profiles for $Sr_{1.4}Ca_{0.6}MnGaO_5$ at 4.2 K with the magnetic peaks circled.

Table 10

Refined magnetic structure of $Sr_{1.4}Ca_{0.6}MnGaO_5$ from low temperature NPD data

Atom	X	Y	Z	Ui/Ue*100	Site	Mult	Fraction (fixed)
Sr	0.1122(8)	0.5148(4)	0.0228(4)	0.296(25)	1	8	0.7000
Mn	0.0000	0.0000	0.0148(9)	0.21(4)	2(001)	4	1
Ga	0.2500	0.07215(3)	0.0653(4)	0.301(34)	M(100)	4	1
O1	0.0062(1)	0.24868(5)	0.2733(5)	0.155(2)	1	8	1
O2	0.1443(1)	-0.0467(3)	0.0000	0.454(26)	1	8	1
O3	0.2500	0.37502(4)	0.9108(5)	0.577(44)	M(100)	4	1
Ca	0.1122(8)	0.51485(4)	0.0228(4)	0.296(25)	1	8	0.3000

R_{wp} = 4.88%, R_P = 4.12%, χ^2 = 8.720

a = 5.3349(1) Å, *b* = 15.8880(5) Å, *c* = 5.4969(1) Å

Cell Volume = 465.925 (19) Å ^{3}

$Sr_{1.5}Ca_{0.5}MnGaO_5$ 'as synthesized'

Low temperature 4.2 K

Figure 25a and **b** show the room temperature and low temperature data respectively. The refinement of these data was performed in a similar way to the previous section using the magnetic space group *Ib'm2* with the moment in the z direction. **Table 11** shows the refined parameters.

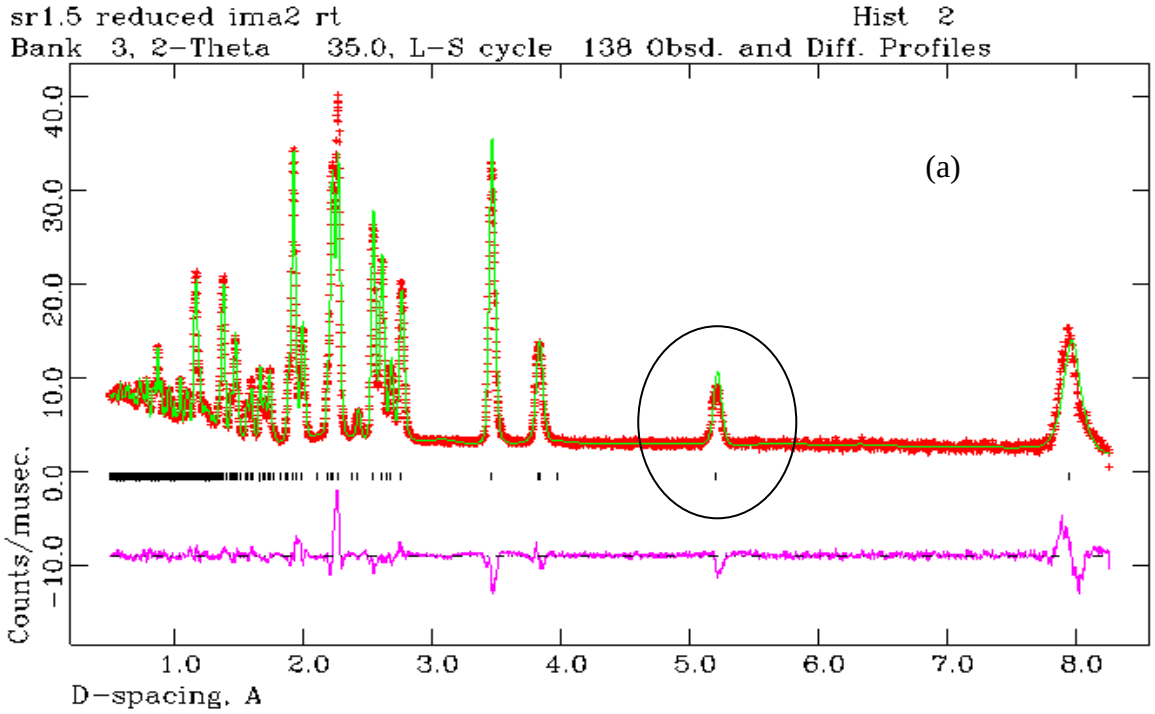

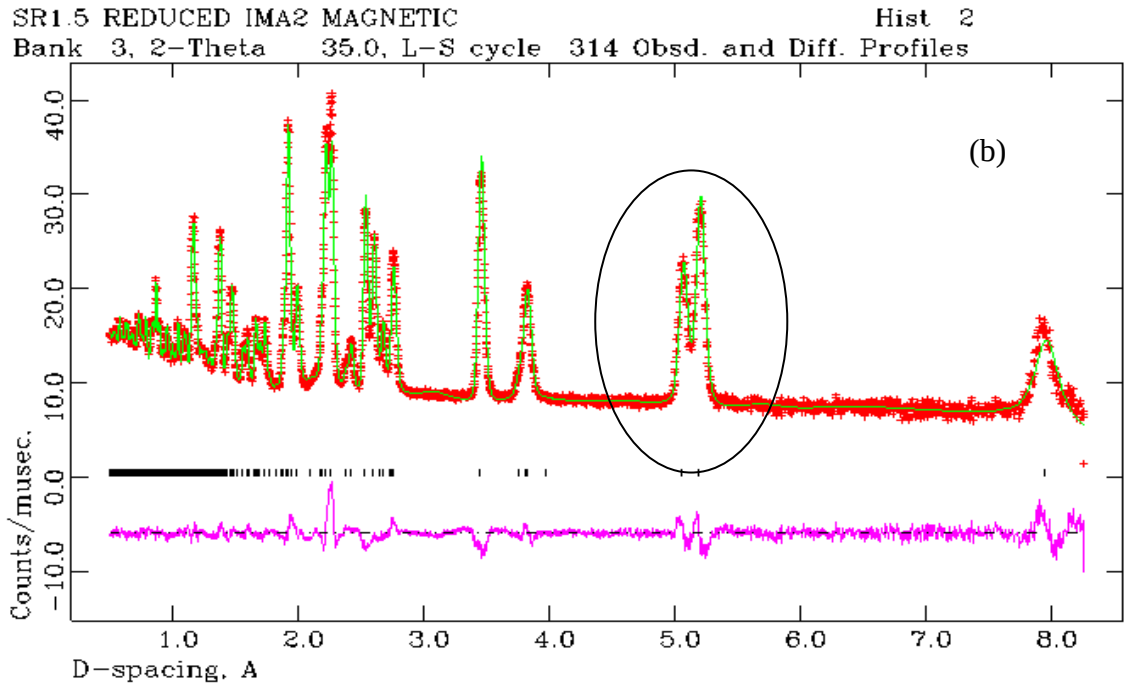

Figure 25 (a) NPD profiles for $Sr_{1.5}Ca_{0.5}MnGaO_5$ collected at room temperature peak circled at 5.2 Å D-spacing, (b) NPD data profiles for $Sr_{1.5}Ca_{0.5}MnGaO_5$ at 4.2 K with the magnetic peaks circled.

Table 11

Refined magnetic structure of $Sr_{1.5}Ca_{0.5}MnGaO_5$ from low temperature NPD data

Atom	X	Y	Z	Ui/Ue*100	Site	Mult	Fraction (fixed)
Sr	0.11225(7)	0.51458(2)	0.0217(4)	0.159(3)	1	8	0.750
Mn	0.0000	0.0000	0.0162(1)	0.45(5)	2(001)	4	1
Ga	0.2500	0.07171(3)	0.0651(4)	0.308(3)	M(100)	4	1
O1	0.0058(1)	0.24854(5)	0.2725(5)	0.142(9)	1	8	1
O2	0.1437(1)	-0.0453(2)	0.0000	0.411(6)	1	8	1
O3	0.250000	0.37338(4)	0.9104(5)	0.557(4)	M(100)	4	1
Ca	0.11225(7)	0.51457(3)	0.0217(4)	0.159(3)	1	8	0.250

R_{wp} = 2.61% R_P = 4.25% χ^2 = 8.872

a = 5.3377(6) Å, *b* = 15.8997(5) Å, *c* = 5.4983(9) Å

Volume = 466.643 (2) Å ^{3}

Figure 26 shows the structure with the direction of the magnetic moments of the manganese represented by arrows. This was applicable to all samples studied i.e $Sr_{2-x}Ca_xMnGaO_5$ $0.5<x<0.7$ modelled with space group *Ib'm2* at room temperature.

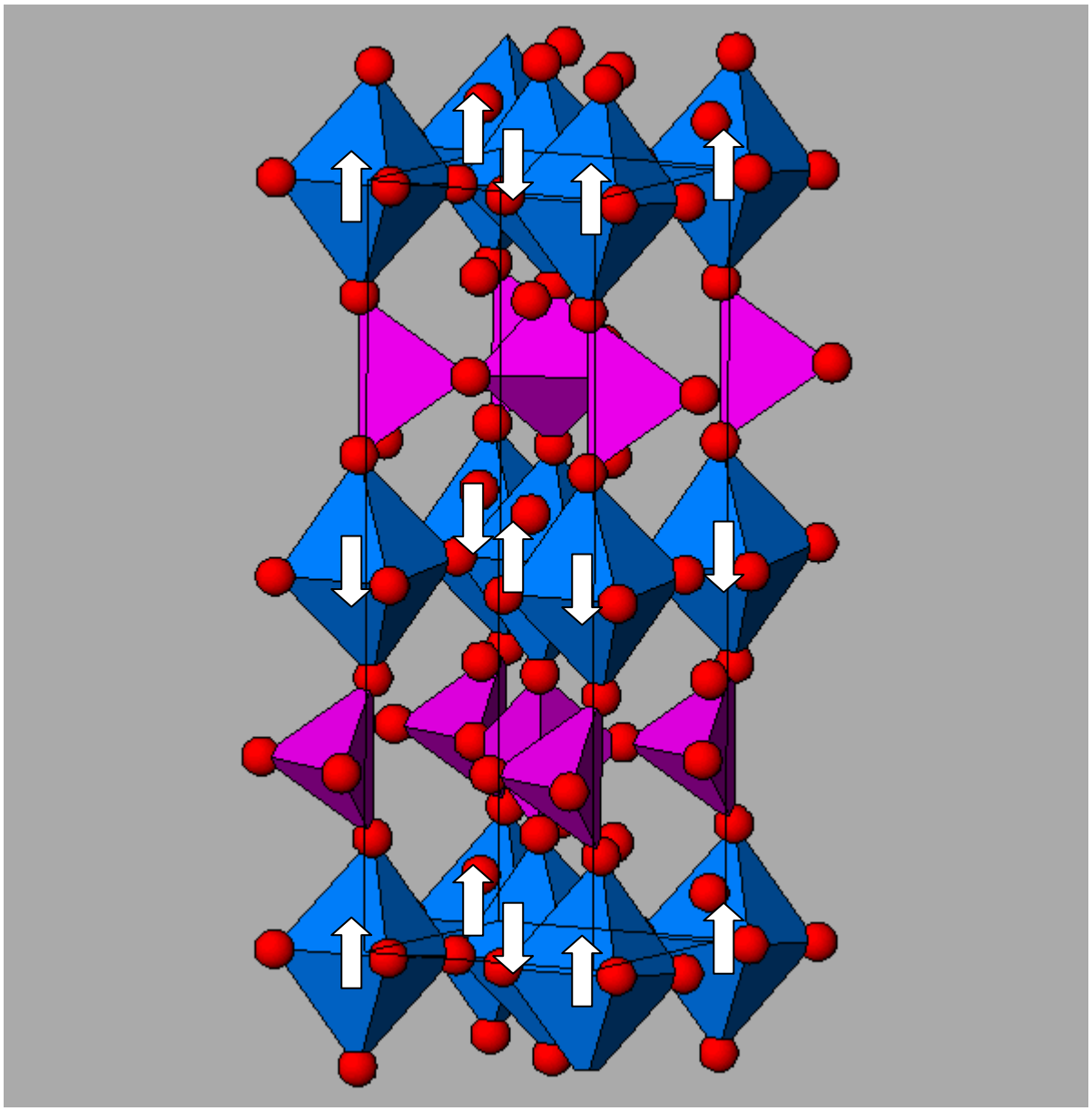

Figure 26

Antiferromagnetic structure of $Sr_{1.5}Ca_{0.5}MnGaO_5$

3.5.2 Bond distances and angles at room temperature

Bond lengths and angles have been collected in **table 12** and **13**, and **figure 27** defines the oxygen numbering. On inspection of bond distances, the most significant bonds to be considered are those involving the GaO_4 tetrahedra and MnO_6 octahedra. As is clearly apparent there is evidence of a Jahn Teller elongation existing in the manganese octahedra.

Table 12

Table of Bond lengths

$Sr_{2-x}Ca_xMnGaO_5$	X= 0.7 Length (Å)	X=0.65 Length (Å)	X=0.6 Length(Å)	X=0.5 Length (Å)
O1-Sr/Ca	2.582 (5) 2.647 (5)	2.5879 (2) 2.6438 (2)	2.5923 (2) 2.6466 (2)	2.5984 (3) 2.6549 (2)
O2-Sr/Ca	2.4398 (3) 3.160 (4)	2.4619 (1) 3.1412 (1)	2.4683 (2) 3.1334 (2)	2.4791 (2) 3.1250 (2)
O3-Sr/Ca	2.3986 (3)	2.3992 (1) 3.6958 (2)	2.3984 (2) 3.6971 (2)	2.3988 (2) 3.6940 (2)
O1-Mn	1.893 (3) 1.945 (3)	1.9022 (3) 1.9382 (4)	1.904 (4) 1.936 (4)	1.9314 (4) 1.9144 (4)
O2-Mn	2.3051 (3)	2.3005 (1)	2.2979 (2)	2.2991 (2)
Bond Valence Sum:O1,O2-Mn	+3.07	+3.06	+3.07	+3.04
O2-Ga	1.8330 (3)	1.8389 (1)	1.8375 (1)	1.8443 (2)
O3-Ga	1.850 (5)	1.8639 (2)	1.8667 (2)	1.8609 (3)
Bond Valence Sum:O2,O3-Ga	+3.08	+2.88	+2.88	+2.87

The bond distances between the manganese and O1 and O2 decrease going from x=0.7 to x=0.5. With the Sr/Ca-O1 bond lengths there is a general increase going from x=0.7 to x=0.5. This matches the increase in Sr content. There is a general increase in both the tetrahedra and octahedra bond lengths again as a result of the larger cell required to accommodate the increased Sr content.

It is interesting to note that in this range the two Mn-O1 distances become more dissimilar as Ca content increases. The longer Mn-O2 bond does not change significantly over the range. Overall the coordination, as measured by Bond Valence sum [41] (BVS) does not change from that expected for a Mn^{3+} ion. Clearly the structure shows local changes to accommodate the smaller Ca whilst retaining the appropriate Mn^{3+} environment. The BVS calculations for the Ga site are consistent with a Ga^{3+} valency. There is a slight reduction to below 3+ for the higher Sr contents and this is likely to be linked with the increased oxygen uptake in these samples, as the oxygens will enter the Ga-O layers.

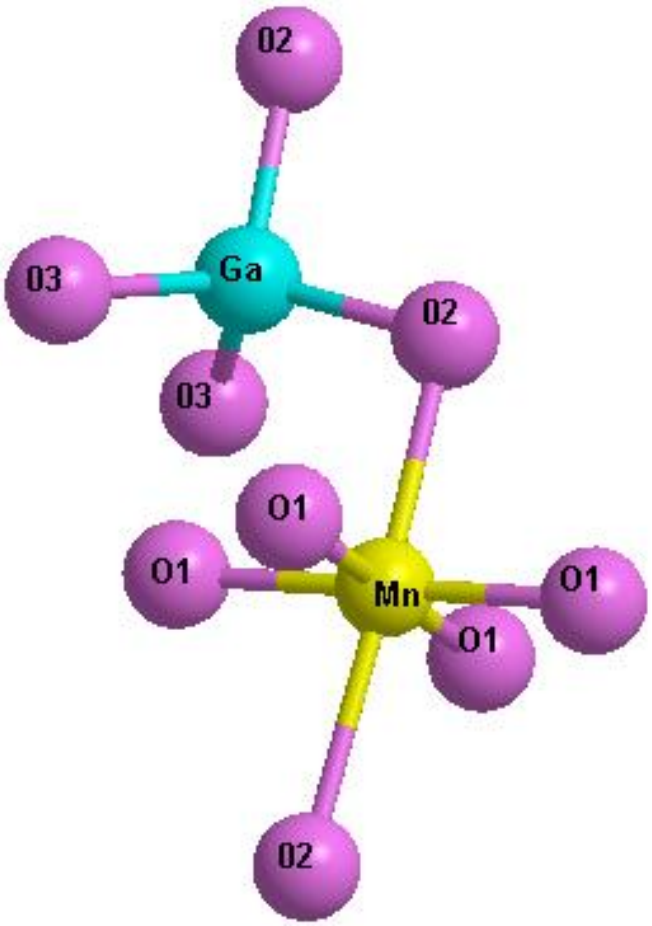

Figure 27
Model of octahedra (Mn) and tetrahedra (Ga)
showing relevant atoms

Table 13

Table of bond angles RT

$Sr_{2-x}Ca_xMnGaO_5$	X= 0.7	X=0.65	X=0.6	X=0.5
O1-Mn-O1	88.055 (3) 176.4 (6)	88.122 (6) 178.40 (2)	88.142 (7) 178.55 (2)	88.182 (6) 178.95 (3)
O1-Mn-O2	87.23 (2) 92.62 (2)	86.75 (2) 93.23 (1)	86.78 (1) 93.20 (1)	86.63 (1) 93.35 (1)
O2-Mn-O2	177.2 (5)	175.39 (2)	175.42 (2)	175.08 (2)
O2-Ga-O3	66.36 (1) 81.08 (1) 104.27 (1)	103.77 (6) 103.90 (5) 122.78 (5)	67.38 (5) 103.52 (6) 122.70 (5)	67.68 (6) 103.32 (7) 103.82 (7)
O3-Ga-O3	108.00 (2)	107.49 (8)	107.20 (9)	107.02 (1)
O2-Ga-O2	88.26 (2) 131.12 (2) 138.77 (1)	87.59 (5) 132.30 (9) 138.55 (5)	87.28 (6) 132.89 (1) 138.34 (6)	86.85 (6) 133.51 (1) 138.15 (2)

3.6 Summary of neutron study

From the results table and values of chi^2 it can be noted that neutron data confirms that the best space group for this composition range (x=0.5-0.7) is *Ibm2*. The space groups of the rest of the range can be validated from literature. Composition x=1 was reported by Battle et al [22] where the space group was confirmed to be *Ibm2.* This is in agreement with the range studied in this report. **Table14** shows the space groups which best fit the structures with the corresponding analytical techniques used.

Table 14

Neutron : samples from this study

$Sr_{2-x}Ca_xMnGaO_5$	Analytical Technique	Space group
x=0	NPD	Icmm [1]
x=0.2	XRD	Icmm
x=0.4	XRD	Ibm2
x=0.5	**NPD**	Ibm2
x=0.6	**NPD**	Ibm2
x=0.65	**NPD**	Ibm2
x=0.7	**NPD**	Ibm2
x=0.8	XRD	Ibm2
x=1	NPD	Ibm2 [24]
x=1.2	XRD	Ibm2
x=1.4	XRD	Pcmn
x=2	NPD	Pcmn [19]

The pure strontium phase has been confirmed to adopt the *Icmm* space group whereas the pure calcium phase has also been confirmed to show the *Pcmn* space group using XRD. This work also agrees with the data in the literature.[19]

The lattice parameters and bond lengths increase progressing from x=2 to x=0. This indicates the unit cell is increasing with higher strontium content.

Magnetic peaks are observed in the low temperature data of the samples studied. The magnetic behaviour of the reduced phase of x=0.5 seems to be canted antiferromagntic with a Neel temperature of 162 K. This is in agreement with the x=1 ratio and x=2 which shows the same behaviour and similar Neel temperatures. The x=0 composition does not however show this behaviour and instead exhibits an indistinct form of antiferromagnetism, with a different space group.

It has been found the intermediate region takes up oxygen quite readily. $Sr_{1.35}Ca_{0.65}MnGaO_5$ has been found to be the most interesting as it takes up a considerable amount compared to $Sr_{1.3}Ca_{0.7}MnGaO_5$ which virtually takes up zero oxygen. Unfortunately, the structures of the oxidised forms of these stoichiometries have been difficult to analyse and characterise. Although the XRD data suggested a single oxidised product, neutron data suggest that at least two phases may have been formed in the oxidation. This may explain why we do not see evidence of ferromagnetic behaviour. Instead of a homogenous sample, we may have produced phases within the sample that are Mn^{3+} rich or Mn^{4+} rich. It is possible the Mn^{3+} ions are situated in a calcium rich phase and Mn^{4+} ions are situated in a strontium rich phase. If this is the case then we would not expect there to be interesting properties in these phases. Further work is required to understand this oxidation process and the products obtained.

4 Conclusion

A range of stoichiometries in $Sr_{2-x}Ca_xMnGaO_5$ (X=0-2) have been studied. Qualitative analysis has been carried out on these samples. Neutron diffraction confirmed space groups of X=0.5, 0.6, 0.65 and 0.7 to be the *Ibm2*. The lattice parameters and volume of unit cell has also been reported. The aim was to investigate the oxidised sample of the same stoichiometries, however they have not shown to be of much significance in this study. This is shown in the XRD scans, which show little change in the structure. There is an extra peak that appears in the scan and neutron diffraction does not show any homogeneous insertion of oxygen into structure. The oxygen's may have been introduced in a random arrangement. There may be clusters of extra oxygen in the structure instead of a repeated crystalline pattern. This would suggest that the sample may not be able to be oxidised in the way predicted.

Further Work

It would be useful to carry out neutron diffraction on the range above X=0.5 to 0.1. This can be studied further to establish the space groups of this range, as it has not been characterised before. MR experiments can be carried out on these samples to investigate MR properties. This can be done using relevant analytical techniques available at the school of physics to measure MR. Further work is required to understand the oxidation process and the products obtained.

References

[1] A. J Wright, H, M Palmer, C. Greaves, P. A Anderson, *J. Mater. Chem*, 11, 1324, 2001
[2] V Pomjakushin, D Sheptvakov, P Fisher, *J. Magnetism and Magnetic Mater*,272, 820-822, 2004
[3] S. Jin, T. H Tiefel, M. McConnack, R.A Fastnactt, R. Ramesh, L.H Chen, *Science*, 264, 413, 1994
[4] G. H Jonker, J. H. Van Santen, *Physica*, 16, 337, 1950
[5] E. O Wollan, W. C Koehler, *Phys. Rev*, 100, 545, 1955
[6] B.R.K Nanda, S. Satpathy, *Physical Review B*, 78, 054427, 2008
[7] P.K Siwach, H.K Singh, O.N Srivastava, *J. Phys. Condens. Matter*, 20, 201, 2008
[8] R. Tetean , I. G. Deac, E. Burzo, A. Berzergheanu, *Jour. Mag. Mater*. 320, 179-182, 2008
[9] S. Yunoki, E. Dagotto. *Phys rev b*, 78, 024405, 2008
[10] D. Akahoshi, R Hatakeyama, H Kuwahara, *Physica B* 403, 1598-1600, 2008
[11] W.C. Hansen, L.T.Brownmiller, R.H. Bouge, *J. Am. Chem*. Soc. 50, 396, 1928
[12] R. Arpe, R Von Schenk, H. Mueller-Buschbaum. *Allg. Chem*, 410, 97, 1974
[13] C. Greaves, AJ Jacobsen, B.C Tofield, *Acta Cryst. B*, 31, 641, 1975
[14] O.H Hansteen, H Fjellvag, B.C Hauback. *J. Sol. Stat. Chem*, 141, 411, 1998
[15] T. Takeda, Y Yamaguchi, H Watanabe, *J. Phys. Soc. Jpn*, 33, 970, 1972
[16] S.B Adler, J.A Reimer, J Baltisberger, U Werner. *Amm. Chem. Soc*, 116, 2, 675, 1994
[17] A.J Wright, personal communication
[18] T. Krekels, O. Milat, G. Van Tendeloo, A. J Wright, C.Greaves, *J. Sol. Stat. chem*, 105, 313, 1993
[19] A. J Wright, H. M Palmer, C. Greaves, P.A. Anderson, *J. Mater. Chem*, 12, 978, 2002
[20] A. M Abakumov, M.G Rozova, B. Ph Pavlyuk, M.V Lobanov, E.V Antipov, O.L Lebedev, G.Van Tendeloo, D. V Sheptyakov, A.M Balagurov, F. Bourée, *J. Sol. State. Chem*. 158, 1,100, 2001
[21] P. Berasteguie, S.G Eriksson, S. Hull,, *Mater.Res. Bull*, 34, 303, 1999
[22] P. D Battle, A. M Bell, S. J Blundell, A.I Coldea, D.J Gallon, F.L Pratt, M.J Rosseinsky, C.A Steer, *J. Sol. state. chem*.. 167, 188, 2002
[23] C. Greaves, A.J Jacobson, B.C Tofield, *Acta crysallogr. Sect B*, 31, 641, 1975
[24] H.M. Palmer, A. Snedden, A.J Wright, C. Greaves, *Chem. Mater*, 18, 1130, 2006
[25] A.M Abakumov, M.G Rozova, B. Ph Pavlyuk, M.V Lobanov, E.V Antipov, O.I Lebedev, G.Van Tendeloo, O.L Ignatchik, E.A Ovtchenkov, A. Koksharov, Yu. A.N Vasil'ev, *J. solid. State, chem*, 160,1, 353, 2001
[26] J. Hadermann, A. M Abakumov, H. D'Hondt, A.S Kalyuzhnaya, M.G Rozova, M. M. Markina, M. G Mikheev, N. Tristan, R. Klingeler, B. Büchner, E.V. Antipov, *J.Mater.Chem.*17,7,692-698,2007
[27] A.M Abakumov M.G Rosova, E.V Antipov, *Russian. Chem, Rev,* 73, 9, 917-931, 2004
[28] B.Lazic, H Kruger, H Kahlenberg, *Acta crys sect B-struc*, 64, 417-425, 2008
[29] Al. Rykov, K Nomura, Y Ueda. *J Magnetism and Magnetic Mater*, 320, 6, 950-956, 2008
[30] M. Zotzl, H Pollmann, *J Amm Cer Soc*, 89, 11, 3491-3497, 2006
[31] E. V Antipov, A. M Abakumov, , A. M Alekseeva, M. G Rozova, J Hadermann, O.L Lebedev, G. Van Tendeloo, *Physica. Stat. Sol. App. Res*, 201, 7, 1403-1409, 2004
[32] J Weissbart, R. Ruka, *electrochem. soc*, 109, 8, 723-726, 1962
[33] S. C. Singhal, *MRS bull*, 25, 3, 16-21, 2000
[34] A Rolle, R.N Vannier, N.V Giridharan. *Solid state ionics*, 176, 25, 2095-2103, 2005
[35] Adapted from figure 3 in the link: http://science.nasa.gov/headlines/y2003/18mar_fuelcell.htm
[36] R Rashid, Project report, *Sch of Chem, Univ of Bham*. 2006
[37] Pecharsky, Zavalij. Fundamentals of Powder diffraction and structural Characterisation on materials,
[38] A.C. Larson and R.B. Von Dreele, *General Structure Analysis System (GSAS*), Los Alamos National Laboratory Report LAUR 86-748, 1994.
[39] H.M Rietveld. *Acta Crystallogr*,22,151-2, 1967
[40] S.J Blundell, J.A Stride, M.L Brooks, *J. Phy, Cond. Matt*, 17, 1, 99-104, 2005
[41] I. D Brown, D, Altermatt, Acta Cryst, B41, 244, 1985

Appendix

TGA data

$Sr_{1.4}Ca_{0.6}MnGaO_5$

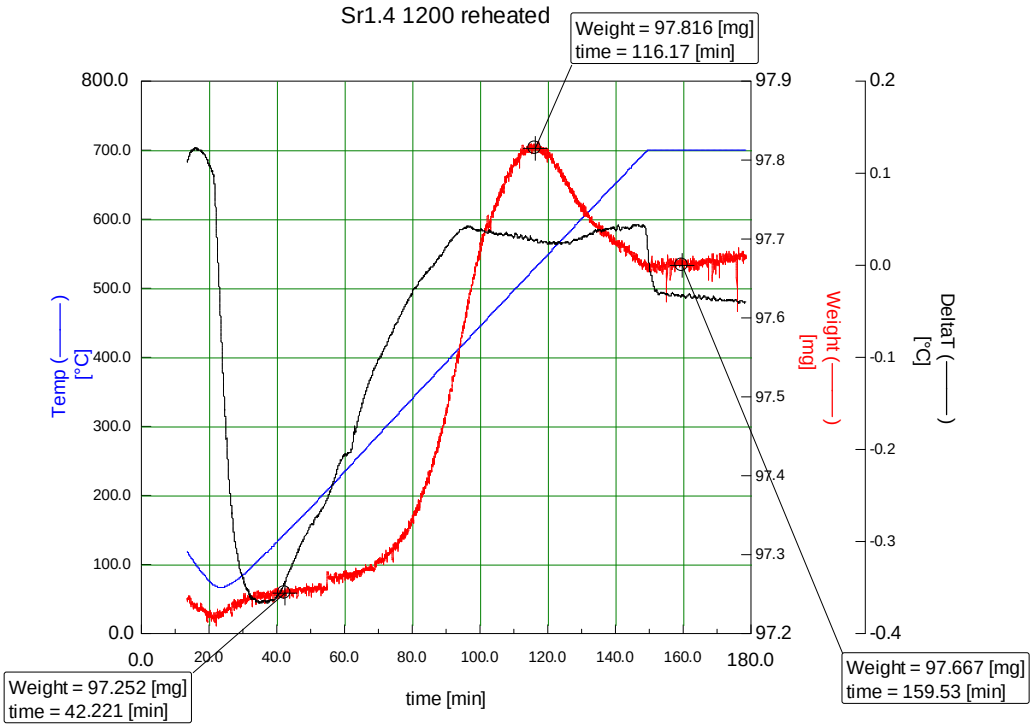

$Sr_{1.35}Ca_{0.65}MnGaO_5$

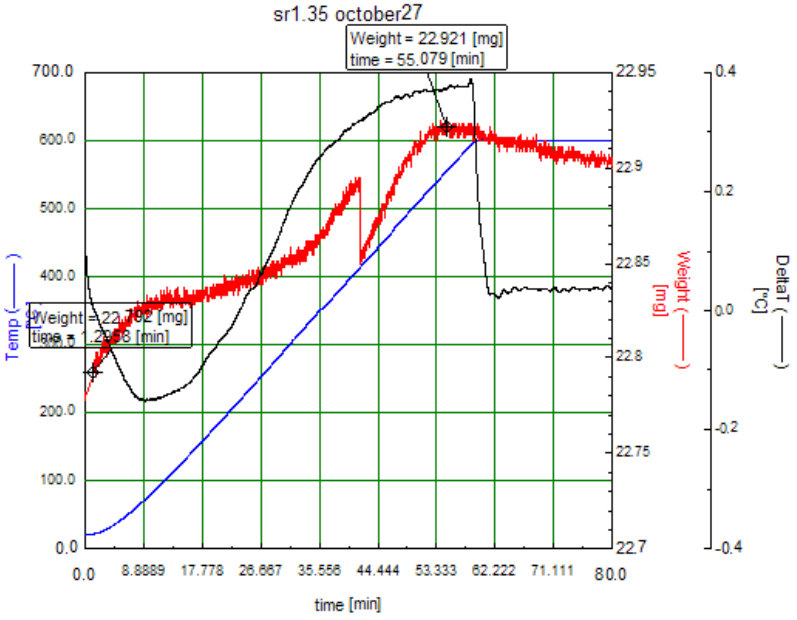

$Sr_{1.3}Ca_{0.7}MnGaO_5$

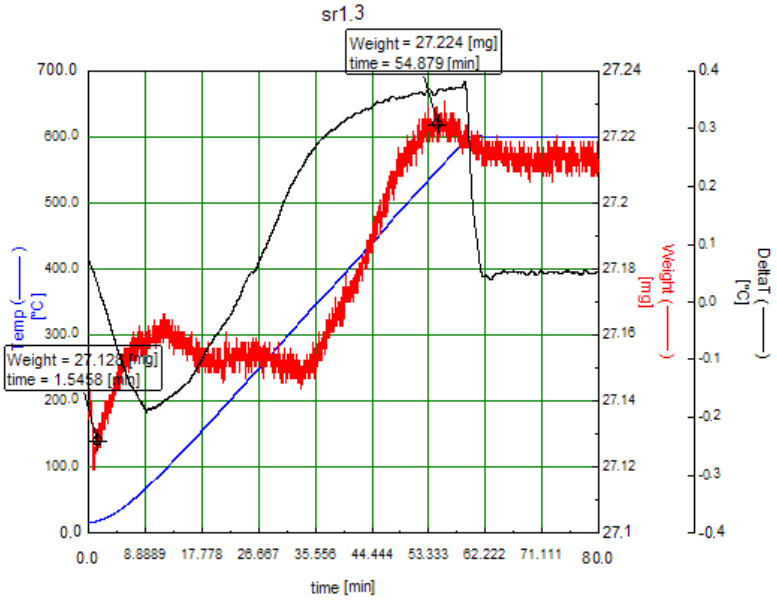

XRD data

Sr2 MnGaO5 74
CELL PARAMETERS AFTER CYCLE 5

	A	B	C	ALPHA	BETA	GAMMA	ABS	ZERO
INIT :	5.396246	16.210624	5.525401	89.999997	89.999997	89.999997	0.000000	-0.063149
FINAL :	5.396246	16.210624	5.525401	89.999997	89.999997	89.999997	0.000000	-0.063149
ESD :	0.002172	0.006678	0.002464	0.000000	0.000000	0.000000	0.000000	0.015888

****

2THET(O)	2THET(C)	H	K	L	D(O)	D(C)	DIF	WEIGHT	SIN**2(O-C)
10.859	10.844	0	2	0	8.141	8.152	0.011	.10E+01	0.00003
16.884	16.876	0	1	1	5.247	5.249	0.002	.10E+01	0.00002
22.953	22.940	0	3	1	3.872	3.874	0.002	.10E+01	0.00005
25.484	25.473	1	2	1	3.492	3.494	0.001	.10E+01	0.00004
31.939	31.929	1	4	1	2.800	2.801	0.001	.10E+01	0.00005
32.288	32.317	0	0	2	2.770	2.768	-0.002	.10E+01	-0.00013
33.098	33.114	2	0	0	2.704	2.703	-0.001	.10E+01	-0.00007
36.890	36.879	1	1	2	2.435	2.435	0.001	.10E+01	0.00006
39.376	39.379	0	4	2	2.286	2.286	0.000	.10E+01	-0.00002
40.051	40.054	2	4	0	2.249	2.249	0.000	.10E+01	-0.00002
40.667	40.666	1	6	1	2.217	2.217	0.000	.10E+01	0.00000
44.619	44.622	0	8	0	2.029	2.029	0.000	.10E+01	-0.00002
46.977	46.976	2	0	2	1.933	1.933	0.000	.10E+01	0.00001
48.381	48.374	2	2	2	1.880	1.880	0.000	.10E+01	0.00004

WAVELENGTH FOR THE ABOVE LINES IS 1.54060

R FACTOR 0.00000004

****

FINAL VALUES AFTER CORRECTING FOR ZERO-POINT ERROR

****

sr1_6MnGaO5 46
CELL PARAMETERS AFTER CYCLE 5

	A	B	C	ALPHA	BETA	GAMMA	ABS	ZERO
INIT :	5.355952	15.982536	5.518799	89.999997	89.999997	89.999997	0.000000	-0.032495
FINAL :	5.355952	15.982535	5.518798	89.999997	89.999997	89.999997	0.000000	-0.032498
ESD :	0.001999	0.005704	0.001746	0.000000	0.000000	0.000000	0.000000	0.014338

****

2THET(O)	2THET(C)	H	K	L	D(O)	D(C)	DIF	WEIGHT	SIN**2(O-C)
11.044	11.030	0	2	0	8.005	8.015	0.010	.10E+01	0.00002
16.949	16.951	0	1	1	5.227	5.226	-0.001	.10E+01	0.00000
23.153	23.155	0	3	1	3.839	3.838	0.000	.10E+01	-0.00001
25.668	25.667	1	2	1	3.468	3.468	0.000	.10E+01	0.00001
32.278	32.260	1	4	1	2.771	2.773	0.002	.10E+01	0.00009
33.402	33.401	2	0	0	2.680	2.681	0.000	.10E+01	0.00000
37.023	37.016	1	1	2	2.426	2.427	0.000	.10E+01	0.00004
39.625	39.630	0	4	2	2.273	2.272	0.000	.10E+01	-0.00003
40.467	40.486	2	4	0	2.227	2.226	-0.001	.10E+01	-0.00011
41.152	41.167	1	6	1	2.192	2.191	-0.001	.10E+01	-0.00009
45.327	45.326	0	8	0	1.999	1.999	0.000	.10E+01	0.00001
47.225	47.228	2	0	2	1.923	1.923	0.000	.10E+01	-0.00002
48.125	48.110	2	6	0	1.889	1.890	0.001	.10E+01	0.00010
48.664	48.661	2	2	2	1.870	1.870	0.000	.10E+01	0.00002
52.557	52.558	0	3	3	1.740	1.740	0.000	.10E+01	0.00000

WAVELENGTH FOR THE ABOVE LINES IS 1.54060

R FACTOR 0.00000004
****
FINAL VALUES AFTER CORRECTING FOR ZERO-POINT ERROR
****
****

sr1.5 MnGaO5 46
CELL PARAMETERS AFTER CYCLE 5

	A	B	C	ALPHA	BETA	GAMMA	ABS	ZERO
INIT :	5.350733	15.922823	5.512909	89.999997	89.999997	89.999997	0.000000	-0.032889
FINAL :	5.350733	15.922823	5.512910	89.999997	89.999997	89.999997	0.000000	-0.032887
ESD :	0.002249	0.006210	0.002440	0.000000	0.000000	0.000000	0.000000	0.015440

****

2THET(O)	2THET(C)	H	K	L	D(O)	D(C)	DIF	WEIGHT	SIN**2(O-C)
11.056	11.072	0	2	0	7.996	7.985	-0.011	.10E+01	-0.00003
16.970	16.973	0	1	1	5.221	5.220	-0.001	.10E+01	-0.00001
23.207	23.212	0	3	1	3.830	3.829	-0.001	.10E+01	-0.00002
25.710	25.706	1	2	1	3.462	3.463	0.000	.10E+01	0.00001
32.356	32.337	1	4	1	2.765	2.766	0.002	.10E+01	0.00009
33.440	33.434	2	0	0	2.677	2.678	0.000	.10E+01	0.00003
37.055	37.058	1	1	2	2.424	2.424	0.000	.10E+01	-0.00002
39.703	39.710	0	4	2	2.268	2.268	0.000	.10E+01	-0.00004
40.549	40.564	2	4	0	2.223	2.222	-0.001	.10E+01	-0.00008
45.507	45.505	0	8	0	1.992	1.992	0.000	.10E+01	0.00001
47.284	47.279	2	0	2	1.921	1.921	0.000	.10E+01	0.00003

WAVELENGTH FOR THE ABOVE LINES IS 1.54060

R FACTOR 0.00000002
****
FINAL VALUES AFTER CORRECTING FOR ZERO-POINT ERROR
****
****

sr1-4MnGaO5 46
CELL PARAMETERS AFTER CYCLE 5

	A	B	C	ALPHA	BETA	GAMMA	ABS	ZERO
INIT :	5.341423	15.903493	5.506651	89.999997	89.999997	89.999997	0.000000	-0.019307
FINAL :	5.341423	15.903493	5.506651	89.999997	89.999997	89.999997	0.000000	-0.019306
ESD :	0.002983	0.008035	0.003163	0.000000	0.000000	0.000000	0.000000	0.020411

****

2THET(O)	2THET(C)	H	K	L	D(O)	D(C)	DIF	WEIGHT	SIN**2(O-C)
11.087	11.099	0	2	0	7.974	7.966	-0.008	.10E+01	-0.00002
17.006	17.007	0	1	1	5.210	5.209	0.000	.10E+01	0.00000
23.245	23.253	0	3	1	3.824	3.822	-0.001	.10E+01	-0.00003
25.754	25.757	1	2	1	3.456	3.456	0.000	.10E+01	-0.00001
32.417	32.395	1	4	1	2.760	2.761	0.002	.10E+01	0.00010
33.503	33.508	2	0	0	2.673	2.672	0.000	.10E+01	-0.00002
35.430	35.408	2	2	0	2.532	2.533	0.002	.10E+01	0.00011
37.116	37.120	1	1	2	2.420	2.420	0.000	.10E+01	-0.00002
39.769	39.772	0	4	2	2.265	2.265	0.000	.10E+01	-0.00002
40.622	40.644	2	4	0	2.219	2.218	-0.001	.10E+01	-0.00013
41.351	41.360	1	6	1	2.182	2.181	0.000	.10E+01	-0.00005
45.583	45.577	0	8	0	1.988	1.989	0.000	.10E+01	0.00004
47.370	47.365	2	0	2	1.918	1.918	0.000	.10E+01	0.00003

WAVELENGTH FOR THE ABOVE LINES IS 1.54060

R FACTOR 0.00000005
****
FINAL VALUES AFTER CORRECTING FOR ZERO-POINT ERROR
****

sr1.35 MnGaO5 46
CELL PARAMETERS AFTER CYCLE 5

	A	B	C	ALPHA	BETA	GAMMA	ABS	ZERO
INIT :	5.334482	15.852248	5.501219	89.999997	89.999997	89.999997	0.000000	-0.038984
FINAL :	5.334481	15.852245	5.501219	89.999997	89.999997	89.999997	0.000000	-0.038987
ESD :	0.001791	0.004832	0.001949	0.000000	0.000000	0.000000	0.000000	0.012385

****

2THET(O)	2THET(C)	H	K	L	D(O)	D(C)	DIF	WEIGHT	SIN**2(O-C)
11.097	11.115	0	2	0	7.967	7.954	-0.013	.10E+01	-0.00003
17.007	17.008	0	1	1	5.209	5.209	0.000	.10E+01	0.00000
23.285	23.284	0	3	1	3.817	3.817	0.000	.10E+01	0.00000
25.781	25.777	1	2	1	3.453	3.453	0.000	.10E+01	0.00001
32.458	32.447	1	4	1	2.756	2.757	0.001	.10E+01	0.00005
33.521	33.533	2	0	0	2.671	2.670	-0.001	.10E+01	-0.00006
37.135	37.143	1	1	2	2.419	2.419	0.000	.10E+01	-0.00004
39.829	39.823	0	4	2	2.261	2.262	0.000	.10E+01	0.00003
40.716	40.705	2	4	0	2.214	2.215	0.001	.10E+01	0.00006
41.450	41.451	1	6	1	2.177	2.177	0.000	.10E+01	0.00000
45.708	45.713	0	8	0	1.983	1.983	0.000	.10E+01	-0.00003
47.402	47.403	2	0	2	1.916	1.916	0.000	.10E+01	-0.00001

WAVELENGTH FOR THE ABOVE LINES IS 1.54060

R FACTOR 0.00000001
****
FINAL VALUES AFTER CORRECTING FOR ZERO-POINT ERROR
****

sr1.3 MnGaO5 46
CELL PARAMETERS AFTER CYCLE 5

	A	B	C	ALPHA	BETA	GAMMA	ABS	ZERO
INIT :	5.336298	15.884506	5.500770	89.999997	89.999997	89.999997	0.000000	-0.027012
FINAL :	5.336297	15.884508	5.500770	89.999997	89.999997	89.999997	0.000000	-0.027013
ESD :	0.002031	0.005613	0.002207	0.000000	0.000000	0.000000	0.000000	0.014018

****

2THET(O)	2THET(C)	H	K	L	D(O)	D(C)	DIF	WEIGHT	SIN**2(O-C)
11.101	11.104	0	2	0	7.964	7.962	-0.002	.10E+01	-0.00001
17.006	17.018	0	1	1	5.210	5.206	-0.004	.10E+01	-0.00003
23.261	23.272	0	3	1	3.821	3.819	-0.002	.10E+01	-0.00004
25.768	25.776	1	2	1	3.455	3.453	-0.001	.10E+01	-0.00003
32.447	32.424	1	4	1	2.757	2.759	0.002	.10E+01	0.00011
33.537	33.534	2	0	0	2.670	2.670	0.000	.10E+01	0.00002
37.155	37.153	1	1	2	2.418	2.418	0.000	.10E+01	0.00001
39.810	39.810	0	4	2	2.263	2.263	0.000	.10E+01	0.00000
40.676	40.680	2	4	0	2.216	2.216	0.000	.10E+01	-0.00003
45.625	45.627	0	8	0	1.987	1.987	0.000	.10E+01	-0.00001
47.406	47.408	2	0	2	1.916	1.916	0.000	.10E+01	-0.00001

WAVELENGTH FOR THE ABOVE LINES IS 1.54060

R FACTOR 0.00000002
****
FINAL VALUES AFTER CORRECTING FOR ZERO-POINT ERROR
****
****

sr1.2 MnGaO5 46
CELL PARAMETERS AFTER CYCLE 5

	A	B	C	ALPHA	BETA	GAMMA	ABS	ZERO
INIT :	5.335453	15.855330	5.497367	89.999997	89.999997	89.999997	0.000000	-0.019311
FINAL :	5.335453	15.855330	5.497368	89.999997	89.999997	89.999997	0.000000	-0.019311
ESD :	0.002497	0.006873	0.002711	0.000000	0.000000	0.000000	0.000000	0.017230

****

2THET(O)	2THET(C)	H	K	L	D(O)	D(C)	DIF	WEIGHT	SIN**2(O-C)
11.110	11.133	0	2	0	7.958	7.941	-0.016	.10E+01	-0.00004
17.035	17.038	0	1	1	5.201	5.200	-0.001	.10E+01	-0.00001
23.304	23.310	0	3	1	3.814	3.813	-0.001	.10E+01	-0.00002
25.801	25.801	1	2	1	3.450	3.450	0.000	.10E+01	0.00000
32.489	32.468	1	4	1	2.754	2.755	0.002	.10E+01	0.00010
33.555	33.547	2	0	0	2.669	2.669	0.001	.10E+01	0.00004
37.183	37.182	1	1	2	2.416	2.416	0.000	.10E+01	0.00001
39.851	39.860	0	4	2	2.260	2.260	0.000	.10E+01	-0.00005
40.701	40.717	2	4	0	2.215	2.214	-0.001	.10E+01	-0.00009
45.726	45.724	0	8	0	1.983	1.983	0.000	.10E+01	0.00002
47.439	47.435	2	0	2	1.915	1.915	0.000	.10E+01	0.00003

WAVELENGTH FOR THE ABOVE LINES IS 1.54060

R FACTOR 0.00000003
****
FINAL VALUES AFTER CORRECTING FOR ZERO-POINT ERROR
****
****

srcA MnGaO5 46
CELL PARAMETERS AFTER CYCLE 5

	A	B	C	ALPHA	BETA	GAMMA	ABS	ZERO
INIT :	5.326738	15.768468	5.497134	89.999997	89.999997	89.999997	0.000000	-0.014017
FINAL :	5.326738	15.768468	5.497134	89.999997	89.999997	89.999997	0.000000	-0.014018
ESD :	0.003040	0.007642	0.003160	0.000000	0.000000	0.000000	0.000000	0.019746

****

2THET(O)	2THET(C)	H	K	L	D(O)	D(C)	DIF	WEIGHT	SIN**2(O-C)
11.217	11.200	0	2	0	7.882	7.894	0.012	.10E+01	0.00003
17.060	17.054	0	1	1	5.193	5.195	0.002	.10E+01	0.00001
23.362	23.383	0	3	1	3.805	3.801	-0.003	.10E+01	-0.00007
25.860	25.852	1	2	1	3.443	3.444	0.001	.10E+01	0.00003
32.563	32.577	1	4	1	2.748	2.746	-0.001	.10E+01	-0.00006
33.620	33.609	2	0	0	2.664	2.664	0.001	.10E+01	0.00006
37.194	37.206	1	1	2	2.415	2.415	-0.001	.10E+01	-0.00006
39.962	39.941	0	4	2	2.254	2.255	0.001	.10E+01	0.00012
41.648	41.648	1	6	1	2.167	2.167	0.000	.10E+01	0.00000
45.994	45.995	0	8	0	1.972	1.972	0.000	.10E+01	-0.00001
47.479	47.484	2	0	2	1.913	1.913	0.000	.10E+01	-0.00003

WAVELENGTH FOR THE ABOVE LINES IS 1.54060

R FACTOR 0.00000003
****
FINAL VALUES AFTER CORRECTING FOR ZERO-POINT ERROR
****

Ca2MnGaO5 62
CELL PARAMETERS AFTER CYCLE 5

	A	B	C	ALPHA	BETA	GAMMA	ABS	ZERO
INIT :	5.272796	15.236862	5.471290	89.999997	89.999997	89.999997	0.000000	-0.022108
FINAL :	5.272795	15.236862	5.471290	89.999997	89.999997	89.999997	0.000000	-0.022112
ESD :	0.002370	0.006058	0.002454	0.000000	0.000000	0.000000	0.000000	0.015094

****

2THET(O)	2THET(C)	H	K	L	D(O)	D(C)	DIF	WEIGHT	SIN**2(O-C)
11.584	11.584	0	2	0	7.633	7.633	0.000	.10E+01	0.00000
17.180	17.184	0	1	1	5.157	5.156	-0.001	.10E+01	-0.00001
23.366	23.390	1	0	1	3.804	3.800	-0.004	.10E+01	-0.00008
23.871	23.864	0	3	1	3.725	3.726	0.001	.10E+01	0.00002
26.182	26.182	1	2	1	3.401	3.401	0.000	.10E+01	0.00000
29.336	29.325	1	3	1	3.042	3.043	0.001	.10E+01	0.00005
32.687	32.687	0	0	2	2.737	2.737	0.000	.10E+01	0.00000
33.272	33.270	1	4	1	2.691	2.691	0.000	.10E+01	0.00001
33.952	33.955	2	0	0	2.638	2.638	0.000	.10E+01	-0.00001
34.504	34.475	2	1	0	2.597	2.599	0.002	.10E+01	0.00014
35.977	35.997	2	2	0	2.494	2.493	-0.001	.10E+01	-0.00010
36.969	36.968	1	0	2	2.430	2.430	0.000	.10E+01	0.00001
37.454	37.452	1	1	2	2.399	2.399	0.000	.10E+01	0.00001
37.796	37.803	1	5	1	2.378	2.378	0.000	.10E+01	-0.00004
41.935	41.938	2	3	1	2.153	2.153	0.000	.10E+01	-0.00002
42.788	42.784	1	6	1	2.112	2.112	0.000	.10E+01	0.00002
47.836	47.837	1	5	2	1.900	1.900	0.000	.10E+01	-0.00001

WAVELENGTH FOR THE ABOVE LINES IS 1.54060

R FACTOR 0.00000004
****
FINAL VALUES AFTER CORRECTING FOR ZERO-POINT ERROR
****
****